Scaling laws for the longitudinal turbulent heat flux in the atmospheric surface layer

K. Y. Huang[1], R. Niraula [1], and G. G. Katul [2,3]

[1]Department of Mechanical and Aerospace Engineering, University of Houston, Houston, Texas, USA
[2]Department of Civil and Environmental Engineering, Duke University, Durham, North Carolina, USA
[3]Department of Civil, Construction, and Environmental Engineering, University of Alabama, Tuscaloosa, Alabama, USA

Key Points:

- New multi-level high frequency measurements on the longitudinal turbulent heat flux near the ground are presented.
- Scaling laws based on similarity theories and directional dimensional analysis are offered.
- A co-spectral budget for the scale-wise evolution of longitudinal heat flux explains contributions from large and inertial scales.

Corresponding author: K. Y. Huang, yhuang68@uh.edu

Abstract

The longitudinal turbulent heat flux is central to the description of vertical momentum and energy transport in stratified atmospheric boundary layers, yet its scaling behavior with respect to thermal stratification remains uncertain in comparison to better-studied quantities such as the vertical heat flux. Here, the scaling laws of the longitudinal heat flux and its co-spectrum in the atmosphere close to the surface as a function of wall normal distance and thermal stratification are experimentally evaluated. Measurements were conducted under varying stability regimes ranging from unstable to slightly stable at two sites. The first experiment included 5 high-temporal resolution (100 Hz) velocity and temperature sensors as well as a triaxial sonic anemometer all positioned within 2 m above a bare soil surface. The second experiment included a single triaxial sonic anemometer positioned at 5 m above the surface of a grass-covered forest clearing. The analysis first examines the Reynolds-averaged Navier–Stokes equations for the longitudinal heat flux and applies similarity theory to identify the dominant terms. This analysis is then used to inform a co-spectral budget, which is used to deduce the appropriate scaling laws at large and inertial subrange scales. The proposed theory aims to reconcile discrepancies reported across field, laboratory, and numerical studies, and highlights the importance of non-conserved scale-wise flux transfer mechanisms unique to longitudinal heat flux in turbulent flows even when the longitudinal heat flux transport term is small.

Plain Language Summary

Swirling motion or eddies in the atmosphere near the ground constantly move heat and momentum horizontally and vertically. These exchanges, which are carried out by eddies that vary appreciably in size and energy content, shape a plethora of processes such as local weather patterns, formation of micro-bursts at airports, or how pollutants and energy spread in the environment. Studies on how eddies move heat vertically to and from the ground is now a mature field when compared to its horizontal (or longitudinal) counterpart. The work here explores theoretically and experimentally through two field experiments how horizontal heat movement by eddies behaves differently under different temperature gradients near the ground. Using new high resolution temperature and velocity data, scaling laws that describe the behavior of horizontal heat transport across different eddy sizes and heights from the ground are derived and tested. The work shows that even when the horizontal heat transport seems small on average, it plays a key role in how eddies distribute energy in the lower atmosphere.

1 Introduction

The longitudinal heat flux $\overline{u'\theta'_v}$ plays a central role in momentum transfer and momentum turbulent fluxes $\overline{w'u'}$ for stratified atmospheric flows, where u', w', and θ'_v are the turbulent longitudinal velocity, turbulent vertical velocity, and turbulent virtual temperature, respectively, and overline is time averaging. The $\overline{u'\theta'_v}$ represents the buoyancy term that acts as a source or a sink in the turbulent momentum flux conservation equation (Garratt, 1992; Mortarini et al., 2025). In non-ideal terrain, $\overline{u'\theta'_v}$ is also needed for modeling all vertical exchanges of heat and momentum in higher-order closure schemes such as those used in climate and weather forecasting (Zeman & Lumley, 1976; J. L. Lumley, 1979; Mellor & Yamada, 1982; Large et al., 1994; Guo et al., 2015). Perhaps the lack of interest in $\overline{u'\theta'_v}$ or its co-spectrum can be traced back to the disproportionate focus on daytime convective boundary layer processes, where the longitudinal heat flux cancels out in the turbulent stress budget (Zilitinkevich et al., 1999; Canuto et al., 1994). Textbooks describing the much studied atmospheric surface layer (ASL) suggest that $\overline{u'\theta'_v} = 0$ for near-neutral and unstable atmospheric stability conditions (Kaimal & Finnigan,

1994). Yet, the relation between $\overline{u'\theta'_v}$ and the vertical heat flux $\overline{w'\theta'_v}$,

$$R_h = -\frac{\overline{u'\theta'_v}}{\overline{w'\theta'_v}}, \tag{1}$$

has been reported for more than 35 years now (Kader et al., 1989; Kader & Yaglom, 1990). It was empirically found that for the near-neutral atmospheric surface layer, the ratio R_h varies between 3 and 4. With increasing instability, the ratio R_h drops to about 0.5 as near-convective conditions are approached. For stable atmospheric stratification, much less is known about the relation between the two heat fluxes except for a few studies (Caughey, 1977). That the signs of $\overline{u'\theta'_v}$ and $\overline{w'\theta'_v}$ are opposite should not be a surprise given the negative correlation between w' and u' in wall-bounded flow.

Models for $\overline{u'\theta'_v}$ benefit from understanding the processes and the scales of motion that contribute to the correlation between u' and θ'_v. In this regard, the state of knowledge for the longitudinal heat flux remains lagging other terms such as the vertical heat flux $\overline{w'\theta'_v}$ or the vertical momentum flux $\overline{w'u'}$ (Panofsky & Mares, 1968). Even in the much studied inertial subrange (ISR) where Kolmogorov scaling is anticipated (Pope, 2000), the scaling laws describing the longitudinal heat flux co-spectrum $F_{u\theta}(k_x)$ as a function of longitudinal wavenumber k_x are not agreed upon. When $F_{u\theta}(k_x)$ is expressed as k_x^{-m} in the ISR (usually identified through velocity spectra), the values of m vary appreciably. The weighty Kansas experiment reports values anywhere from $m = 3$ (J. Wyngaard & Coté, 1972) to $m = 5/2$ (Kaimal et al., 1972) even when the co-spectra for momentum and vertical heat fluxes follow the anticipated $k_x^{-7/3}$. However, the experiments in Minnesota (USA) and Tsimlyansk (Russia) suggest a more conventional $m = 7/3$ (Caughey et al., 1979; Kader & Yaglom, 1991) that agrees with the vertical momentum flux co-spectrum $F_{wu}(k_x)$ (J. Lumley, 1967; G. Katul et al., 2013). Field studies exploring the $F_{wu}(k_x)$ scaling where temperature can be assumed as a passive scalar report an $m = 5/3$ for some 3 decades of k_x before transitioning in a narrow range of scales to $m = 7/3$ followed by an exponential cutoff (Antonia & Zhu, 1994). In contrast, studies in the roughness sublayer of an alpine forest (Cava & Katul, 2012) in Lavarone (Italy) spanning both unstable and mildly stable conditions report $m = 7/3$ for at least two decades of wavenumbers in the ISR. Direct numerical simulations (W. Bos et al., 2004) suggest an $m = 2$ attributing deviations from $m = 7/3$ due to a finite heat flux transfer across scales. Unlike the turbulent kinetic energy dissipation rate ε, the flux transfer associated with the longitudinal heat flux across k_x is not a 'conserved' quantity and can exhibit its own exponents. Direct numerical simulations (DNS) used to calibrate the Eddy-Damped Quasi Normal Model (EDQNM) reveal an $m = 23/9$ (W. J. Bos & Bertoglio, 2007), which is close to the early field studies reporting $m = 5/2$ (Caughey, 1977).

Here, the scaling laws of $\overline{u'\theta'_v}$ and its co-spectrum in the atmosphere very close to a flat surface as a function of wall normal distance and thermal stratification are experimentally evaluated using both single-level sonic anemometer measurements and very high temporal resolution (=100 Hz) u' and θ'_v profile measurements in the atmospheric surface layer (ASL). These measurements were conducted at the Surface Layer Turbulence and Environmental Science Test (SLTEST) facility in western Utah, USA, where the surface is a desert-like dry lake bed covered with salt. Another single-level experiment utilizing conventional sonic anemometry conducted above a grass-covered forest clearing near Durham, North Carolina is also used to assess the robustness of the findings between different sites and surface conditions. The analysis first examines the longitudinal heat flux conservation equation and applies similarity theory and other realizability constraints to identify the dominant terms. This analysis is then used to inform a co-spectral budget, which explores the scaling laws at low and high wavenumbers. A discussion regarding discrepancies reported across field, laboratory, and numerical studies is presented with the aim of illustrating the significance of non-conserved flux transfer mechanisms unique to longitudinal heat flux.

2 Theory

The theory section begins with an overview and the standard conservation equations for the longitudinal heat flux. Those equations are derived from a Reynolds-Averaged Navier-Stokes (RANS) perspective and then combined with scaling arguments to offer first-order estimates on how thermal stratification impacts production, transport, and dissipation of $\overline{u'\theta'_v}$. These scaling arguments cover conventional Monin-Obukhov similarity theory, directional-dimensional analysis, and other possibilities for weakly stable stratification. Existing and new theories for the co-spectrum are then presented using dimensional considerations (W. Bos et al., 2004; W. J. Bos & Bertoglio, 2007; Cava & Katul, 2012), a constant correlation hypothesis that was tested using field studies (Antonia & Zhu, 1994), and a co-spectral budget that links the co-spectrum of the longitudinal heat flux to the better studied co-spectra of momentum and vertical heat fluxes (G. G. Katul et al., 2013; Mortarini et al., 2025).

2.1 Definitions and General Considerations

The coordinate system employed here defines x (or x_1), y (or x_2), and z (or x_3) as the longitudinal (along mean wind direction), lateral, and vertical directions, respectively, with $z = 0$ set at the ground surface. The instantaneous velocity components along these directions are u (or u_1), v (or u_2), and w (or u_3). An overline indicates averaging over coordinates of statistical homogeneity (commonly time averaging in field experiments), and primes denote turbulent fluctuations about the mean (e.g., $u = \overline{U} + u'$). For a stationary and planar homogeneous flow at high Reynolds number in the absence of subsidence, the turbulent longitudinal heat flux conservation equation is (Garratt, 1992; Kaimal & Finnigan, 1994; J. C. Wyngaard, 2010):

$$\frac{\partial \overline{u'\theta'_v}}{\partial t} = 0 = \underbrace{-\overline{w'u'}\,\Gamma_\theta(z) - \overline{w'\theta'_v}\,\Gamma(z)}_{Production} - \underbrace{\frac{1}{\overline{\rho}}\overline{\theta'_v \frac{\partial p'}{\partial x}}}_{Pressure-Decorrelation} - \left[\underbrace{\frac{\partial \overline{w'u'\theta'_v}}{\partial z}}_{Flux-Transport} - \underbrace{D_m \overline{u' \frac{\partial^2 \theta'_v}{\partial x_j \partial x_j}} - \nu \overline{\theta'_v \frac{\partial^2 u'}{\partial x_j \partial x_j}}}_{Molecular-Dissipation} \right], \tag{2}$$

where t is time, u' and w' are the longitudinal (along x) and vertical (along z) velocity fluctuations around their mean states $\overline{U}$ and $\overline{W} = 0$ (no subsidence), θ'_v is the virtual temperature fluctuation around its mean state $\overline{\theta_v}$, $\overline{u'\theta'_v}$ is the horizontal heat flux that can be positive or negative, $\Gamma = \partial\overline{U}/\partial z$ is the mean longitudinal velocity gradient, $\Gamma_\theta = \partial\overline{\theta_v}/\partial z$ is the mean virtual temperature gradient, ρ is the air density, p' is the pressure fluctuations referenced to a hydrostatic state, $\overline{w'u'\theta'_v}$ is the vertical transport of $\overline{u'\theta'_v}$ by turbulence, D_m is the molecular diffusion coefficient for heat in air, and ν is the kinematic viscosity of air. Hereafter, the sum of the two production terms in Equation 2 is labeled as P_m and reflects the interaction between the mean flow and turbulence generating a correlation between u' and θ'_v. For notational simplicity, it is given by

$$P_m = -\left[\overline{w'u'}\,\Gamma_\theta(z) + \overline{w'\theta'_v}\,\Gamma(z)\right]. \tag{3}$$

Due to the presence of a solid boundary, $\overline{w'u'} < 0$, $\Gamma > 0$, and instability is often defined by the sign of $\overline{w'\theta'_v}$ (unstable if positive and stable if negative) or Γ_θ (unstable if negative and stable if positive). Thus, when $\overline{w'\theta'_v} \propto -\Gamma_\theta$, the two terms in P_m act in tandem to support the generation of a correlation between u' and θ'_v.

Standard closure schemes for the pressure-decorrelation are based on a linear Rotta scheme for the so-called 'slow term' modified to include an isotropization of the production of $\overline{u'\theta'_v}$ (or P_m) for the 'fast term' (Launder et al., 1975; Pope, 2000). The appli-

cation of this closure begins by expressing

$$\overline{\theta_v' \frac{\partial p'}{\partial x}} = \frac{\partial \overline{\theta_v' p'}}{\partial x} - \overline{p' \frac{\partial \theta_v'}{\partial x}}.$$

Ignoring the $\partial(.)/\partial x$ term (i.e. the pressure transport term) due to planar homogeneity, and closing the pressure-scalar interaction term using

$$\frac{1}{\overline{\rho}} \overline{\theta_v' \frac{\partial p'}{\partial x}} = -\overline{p' \frac{\partial \theta_v'}{\partial x}} = C_R \frac{\overline{u'\theta_v'}}{\tau_d} - C_I P_m, \tag{4}$$

yields the sought outcome, where $C_I = 3/5$ is a constant associated with the fast isotropization of the production terms P_m and whose numerical value has been derived from Rapid Distortion Theory (Launder et al., 1975; Pope, 2000; G. G. Katul et al., 2013), $C_R = 1.8$ is the Rotta constant associated with the slow pressure-rate-of-strain part (Pope, 2000), and τ_d is a de-correlation time scale that may be related to a relaxation time (to be discussed later). This so-called LRR-IP model (after Launder, Reece, and Rodi including the isotropization of the production) has been chosen because it reproduces the mean velocity and stresses in many shear flows (Pope, 2000; Choi & Lumley, 2001; Durbin, 1993; Launder et al., 1975; Hanjalić & Launder, 2021). The isotropization of the production is assumed to directly apply on P_m in the longitudinal heat flux budget through the action of the fast component of the pressure de-correlation. Inserting this closure into the longitudinal heat flux budget to solve for $\overline{u'\theta_v'}$ yields,

$$\overline{u'\theta_v'} = \frac{\tau_d}{C_R} \left[P_m \left(1 - C_I\right) \; - \left(\frac{\partial \overline{w'u'\theta_v'}}{\partial z} - D_m \overline{u' \frac{\partial^2 \theta_v'}{\partial x_j \partial x_j}} - \nu \overline{\theta_v' \frac{\partial^2 u'}{\partial x_j \partial x_j}} \right) \right], \tag{5}$$

In the standard Rotta closure where $C_R = 1.8$, τ_d must be interpreted as a relaxation (instead of a de-correlation) time and is given by

$$\tau_d = \frac{1}{2} \frac{\left(\overline{u_j' u_j'}\right)}{\varepsilon} \tag{6}$$

where $\overline{u_j' u_j'}/2$ is the turbulent kinetic energy (TKE) and ε is the TKE dissipation rate. Thus, for near-neutral atmospheric stability conditions,

$$\tau_d(z) = \phi_{TKE}(0) \frac{\left(\overline{u_*^2}\right)}{[u_*^3/(\kappa z)]} = \phi_{TKE}(0) \frac{\kappa z}{u_*}, \tag{7}$$

where $\kappa = 0.4$ is the von Karman constant, $\phi_{TKE}(0)$ is a coefficient that links the turbulent kinetic energy (TKE) to u_*^2 for a near-neutral ASL, and $u_* = \sqrt{-\overline{u'w'}}$ is the friction velocity. This scaling for τ_d assumes that (i) the TKE budget is reduced to a balance between shear production and viscous dissipation, such that $\varepsilon \approx -\overline{u'w'}\,\partial\overline{U}/\partial z$, and that under near-neutral conditions $\partial\overline{U}/\partial z \approx u_*/(\kappa z)$, which together yield $\varepsilon \approx u_*^3/(\kappa z)$ (Charuchittipan & Wilson, 2009), and (ii) the TKE follows MOST for near-neutral conditions, which it does not - given that $\overline{u'u'}/u_*^2$ is well predicted by the attached eddy hypothesis for near-neutral conditions and this prediction involves the boundary layer depth (Huang & Katul, 2022). Nonetheless, this estimate of τ_d may be interpreted as the time it takes for turbulence to adjust to any changes in mean flow gradients (especially those associated with P_m).

Two limiting cases of the general budget are considered in what follows to illustrate the connection (or lack thereof) between $\overline{u'\theta_v'}$ and mean flow properties. The first is a balance between production and pressure-decorrelation, which leads to a gradient-diffusion approximation for $\overline{u'\theta_v'}$. The second is a balance between flux transport and pressure-decorrelation, which — as shown below — admits a family of height-dependent solutions.

In the first limiting case, the flux transport term is ignored and the high Reynolds number limit applies, such that molecular processes are less efficient at de-correlating u' from θ'_v than pressure de-correlation. The dominant balance is then between production P_m and pressure-decorrelation (the only remaining covariance destruction term), yielding a flux-gradient relation for the longitudinal heat flux:

$$\overline{u'\theta'_v} = -\frac{1-C_I}{C_R}\tau_d \left[\overline{w'u'}\ \Gamma_\theta(z) + \overline{w'\theta'_v}\ \Gamma(z)\right]. \tag{8}$$

For a strictly neutral limit where $\Gamma_\theta \to 0$ and $\overline{w'\theta'_v} \to 0$, Equation 8 predicts a $\overline{u'\theta'_v} = 0$ because $P_m \to 0$. Likewise, in the free convective limit where $u_*^2 \to 0$ and $\Gamma \to 0$, Equation 8 also predicts $\overline{u'\theta'_v} \to 0$. For this reason, some textbooks list $\overline{u'\theta'_v} = 0$ for near-neutral to unstable atmospheric conditions (Kaimal & Finnigan, 1994) when the flow is stationary, planar homogeneous, and high Reynolds number. These findings (i.e. $P_m \to 0$) are not fully supported by near-neutral and near-convective ASL studies (Bradley et al., 1982; Wilczak & Businger, 1984). Those contradictions may be pointing to the fact that the flux-transport term can be significant. For near-neutral conditions in the ASL, a finite $\overline{w'\theta'_v}$ is common even when buoyancy contributions to the TKE budget are small. It is this finite $\overline{w'\theta'_v}$ that may be of disproportionate significance to the budget of $\overline{u'\theta'_v}$ that is to be explored here as well.

In the second limiting case, the flux transport term is the only term that connects the outer layer to the near-surface heat flux in the absence of any local production of $\overline{u'\theta'_v}$. To estimate the possible role of the flux transport term, at least in a first-order analysis, a gradient-diffusion closure is used for its vertical transport and yields

$$\overline{w'u'\theta'_v} = -K_t(z)\frac{\partial \overline{u'\theta'_v}}{\partial z}. \tag{9}$$

That is, restricting the balance between flux transport and modeled pressure-de-correlation yields an approximated longitudinal heat flux budget given by

$$K_t\frac{\partial^2 \overline{u'\theta'_v}}{\partial z \partial z} + \frac{\partial K_t}{\partial z}\frac{\partial \overline{u'\theta'_v}}{\partial z} - \frac{C_R}{\tau_d}\overline{u'\theta'_v} = 0. \tag{10}$$

In the near-neutral limit, it may be argued that $K_t = \kappa z u_*$, $\tau_d = \phi_{TKE}(0)\kappa z/u_*$, and the budget in Equation 10 becomes

$$z^2\frac{\partial^2 \overline{u'\theta'_v}}{\partial z \partial z} + z\frac{\partial \overline{u'\theta'_v}}{\partial z} - a_n\ \overline{u'\theta'_v} = 0;\ a_n = \frac{C_R}{\kappa^2\phi_{TKE}(0)}. \tag{11}$$

This homogeneous second-order ordinary differential equation is of the Cauchy-Euler form whose general solution is given as

$$\overline{u'\theta'_v} = B_1 z^{a_n} + B_2 z^{-a_n}. \tag{12}$$

The boundary conditions $z \to 0$ and $z \to \infty$ set $B_2 = 0$ and $B_1 = 0$, respectively, yielding the individual contributions to the general solution. For the free convective limit, K_t and τ_d are independent of z (as they vary with the convective boundary layer height) and the budget in Equation 10 reduces to

$$\frac{\partial^2 \overline{u'\theta'_v}}{\partial z \partial z} = a_c\overline{u'\theta'_v};\quad a_c = \frac{C_R}{K_t\tau_d}. \tag{13}$$

The solution is

$$\overline{u'\theta'_v} = C_1\exp(\sqrt{a_c}z) + C_2\exp\left(-\sqrt{a_c}z\right). \tag{14}$$

In the limiting cases where $z \to \infty$, $C_1 = 0$ suggesting that the longitudinal heat flux decays exponentially with increasing z.

These budget considerations suggest that when variations in $\overline{u'\theta'_v}$ with z occur, the flux transport term is likely to be significant and its magnitude is commensurate with the pressure-decorrelation contribution. Conversely, when the z-dependency of $\overline{u'\theta'_v}$ is weak or insignificant, it may be argued that the flux-transport term is small and can be ignored.

2.2 Dimensional Analysis Applied to the Horizontal Heat Flux

2.2.1 A Monin-Obukhov Similarity Theory (MOST) Scaling

It may be instructive to ask what are the scaling laws for $\overline{u'\theta'_v}$ with atmospheric stability in the diabatic atmospheric surface layer (ASL) assuming Monin and Obukhov (Monin & Obukhov, 1954) Similarity theory (MOST) holds for momentum and vertical heat transport. To connect MOST to Equation 8, the following definitions are introduced:

$$\Gamma\frac{\kappa z}{u_*} = \phi_m(\zeta),\ \Gamma_\theta\frac{\kappa z}{T_*} = \phi_h(\zeta),\ Pr_t = \frac{\phi_h(\zeta)}{\phi_m(\zeta)}, \tag{15}$$

where $T_* = -\overline{w'\theta'_v}/u_*$ is a temperature scale, $\zeta = z/L_o$ is the atmospheric stability parameter, L_o is the Obukhov length given by

$$L_o = -\frac{u_*^3}{\kappa\beta\overline{w'\theta'_v}},$$

$\beta = g/\overline{\theta_v}$ is the buoyancy parameter, g is the gravitational acceleration, $\phi_m(\zeta)$ and $\phi_h(\zeta)$ are the stability correction functions for momentum and heat, respectively, and Pr_t is the turbulent Prandtl number with values between 0.7 to 1.0 in the near-neutral limit (Kays, 1994; Li, 2019). Inserting these MOST results into Equation 8 yields

$$\overline{u'\theta'_v} = \left(\frac{1-C_I}{C_R}\right)\left[\tau_d\ \phi_m(\zeta)\right]\frac{u_*^2 T_*}{\kappa z}\left[1+Pr_t(\zeta)\right]; \tau_d = \frac{\kappa z}{u_*}\left[\frac{\phi_{TKE}(\zeta)}{\phi_\varepsilon(\zeta)}\right], \tag{16}$$

where $\phi_\varepsilon(\zeta)$ is the stability correction function for ε presented elsewhere (Hsieh & Katul, 1997). Because a number of studies report the relative importance of horizontal to vertical heat flux, or the ratio R_h (Kader & Yaglom, 1990), Equation 16 is re-casted as

$$R_h = -\frac{\overline{u'\theta'_v}}{\overline{w'\theta'_v}} = \left(\frac{1-C_I}{C_R}\right)\left[\tau_d\ \phi_m(\zeta)\right]\frac{u_*}{\kappa z}\left[1+Pr_t(\zeta)\right]. \tag{17}$$

Inserting Equation 6 into Equation 17 yields an estimate for the ratio R_h based on dimensionless stability correction functions given by

$$R_h = -\frac{\overline{u'\theta'_v}}{\overline{w'\theta'_v}} = \left(\frac{1-C_I}{C_R}\right)\left[\frac{\phi_{TKE}(\zeta)\ \phi_m(\zeta)}{\phi_\varepsilon(\zeta)}\right]\left[1+\frac{\phi_h(\zeta)}{\phi_m(\zeta)}\right]. \tag{18}$$

For small $|\zeta|$ (i.e. near-neutral), setting $Pr_t(0) = 1$, and noting that $C_R = 1.8$, $C_I = 3/5$, $\phi_m(0) = 1$, $\phi_\varepsilon(0) = 1$, $\phi_{TKE}(0) = 6.7$ yields

$$R_h = -\frac{\overline{u'\theta'_v}}{\overline{w'\theta'_v}} = 3.$$

This estimate, which did not involve any 'tunable' parameters, is close to the family of ASL experiments (Kader & Yaglom, 1990) reporting values between 3.5 and 4.0 for near-neutral conditions (especially their Figures 3 and 4). This agreement lends some confidence in the closure scheme employed when sensible heat flux is small but finite (i.e. does not contribute appreciably to the TKE budget) yet the flow remains near-neutral due to a high u_*.

2.2.2 Realizability Constraint on the Longitudinal Heat Flux

That the ratio R_h is larger than unity in magnitude may have been foreshadowed when noting that

$$R_h = -\frac{\overline{u'\theta'_v}}{\overline{w'\theta'_v}} = -\frac{R_{u\theta}}{R_{w\theta}}\frac{\sigma_u}{\sigma_w},$$

where $R_{ab} = \overline{a'b'}/(\sigma_a\sigma_b)$ is the correlation coefficient between two variables (a and b). Since attached eddies or eddies associated with a k_x^{-1} scaling exponent in the spectra of u' and θ'_v for near-neutral conditions (Kader & Yaglom, 1991; G. G. Katul et al., 1995; Huang & Katul, 2022; Huang et al., 2023) contribute to $R_{u\theta}$ but less so to $R_{w\theta}$ (the spectrum of w' is flat for $k_x z < 1$), it is anticipated that $|R_{u\theta}/R_{w\theta}| > 1$. Moreover, $\sigma_u/\sigma_w > 2$ due to the presence of the wall. These considerations alone lead to $|R_h| > 2$.

A further refinement may be achieved from a statistical point of view by considering the correlation coefficients between three arbitrary normalized variables selected here to be u'/σ_u, w'/σ_w, and θ'_v/σ_θ. These three normalized variables can be used to form a symmetric and thus positive-definite matrix A_c. Because it is positive definite, its determinant must be positive and is given by (Bink & Meesters, 1997; G. Katul & Hsieh, 1997; Priestley, 1988)

$$\det(A_c) = \det\begin{bmatrix} 1 & R_{u\theta} & R_{w\theta} \\ R_{u\theta} & 1 & R_{uw} \\ R_{w\theta} & R_{uw} & 1 \end{bmatrix} = 1 + 2R_{uw}R_{u\theta}R_{w\theta} - (R_{u\theta}^2 + R_{w\theta}^2 + R_{uw}^2) \geq 0.$$

This condition, which holds for any symmetric matrix with real-valued finite elements, can now be employed to set an upper bound on $R_{u\theta}$ using the more studied $R_{w\theta}$ and R_{uw}. That is,

$$R_{u\theta} \in R_{uw}R_{w\theta} \pm \sqrt{1 + R_{uw}^2R_{w\theta}^2 - (R_{uw}^2 + R_{w\theta}^2)}, \tag{19}$$

or

$$|R_{u\theta}| \leq |R_{uw}R_{w\theta}| + \sqrt{1 + R_{uw}^2R_{w\theta}^2 - (R_{uw}^2 + R_{w\theta}^2)}. \tag{20}$$

For near-neutral to slightly unstable conditions, $R_{w\theta} = 0.5$ and $R_{uw} = -0.35$ (Kaimal & Finnigan, 1994), thereby bounding $R_{u\theta} \in [-0.99, +0.64]$. Using the lower bound, the corresponding ratio is $R_h = -(-0.99/0.5) \times (2.7/1.25) = 4.4$, which represents an upper limit consistent with the realizability constraint. This value exceeds the prediction of $R_h = 3$ using the closure scheme from Equation 18 under near-neutral limits, and remains close to the experimental value $R_{u\theta} = 4$ reported from long-term field studies for near-neutral conditions (Kader & Yaglom, 1990). These findings offer a plausibility check that the model for R_h in Equation 18, with $C_R = 1.8$, $C_I = 3/5$, and $\phi_{TKE}(0) = 6.7$, is compatible with estimates using other independent flow quantities in the ASL ($R_{w\theta} = 0.5$, $R_{uw} = -0.35$).

2.2.3 A Directional Dimensional Analysis (DDA) for Unstably Stratified Flows

The DDA, pioneered for the ASL in the early 1970s (Betchov & Yaglom, 1971; Zilitinkevich, 1973), was formalized and expanded for unstable conditions in the early 1990s (Kader & Yaglom, 1990). The DDA begins by noting that the generation of TKE occurs from two sources when the atmosphere is unstable: mechanical production ($P_{uu} = -\overline{w'u'}\Gamma$) from $\overline{u'u'}$ injected in the horizontal and buoyancy production ($P_{ww} = \beta\overline{w'\theta'_v}$) from $\overline{w'w'}$ injected in the vertical. DDA also assumes that these two TKE generation mechanisms are, to a leading order, decoupled. It then associates separate horizontal and vertical length scales (L_x and L_z) to each (directional) generation mechanism. Length scales associated with generating u' (through P_{uu}) are characterized by L_x whereas processes generating w' (through P_{ww}) are associated with L_z. A drawback to this approach is that it ignores interactions between these two components that may occur due to pressure redistribution and return to isotropy (Bou-Zeid et al., 2018). Nonetheless, when the

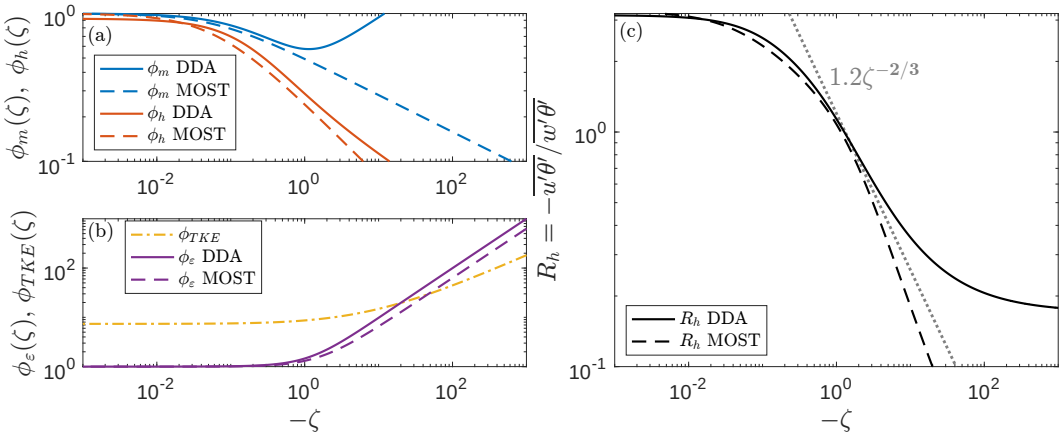

Figure 1. Comparison of DDA and MOST predictions of (a) the stability correction functions ϕ_m and ϕ_h, (b) ϕ_ε, and (c) the ratio $R_h = -\overline{u'\theta'_v}/\overline{w'\theta'_v}$ computed from Equation 18 using functions in panels (a,b). Panel (b) also shows ϕ_{TKE}, computed assuming σ_w/u_* varies with ζ, while $\sigma_u/u_* = 2.7$ and $\sigma_v/u_* = 2.3$ are held constant in the dynamic and dynamic–convective regimes.

generation mechanisms of u' and w' occur at scales much larger than the scales at which return to isotropy becomes effective, the assumptions behind DDA may still hold. Some indirect support for this conjecture was recently reported using ASL experiments in the context of scale-wise return to isotropy of the stress tensor from production to inertial for a large number of atmospheric conditions (Brugger et al., 2018; Stiperski et al., 2021). The DDA further assumes that a single characteristic time t_c (no directional association) exists. Accepting the 'decoupling' between L_x and L_z implies that $u_*^2 = -\overline{u'w'}$ is associated with $L_x L_z t_c^{-2}$. Thus, u_* does not 'qualify' as a horizontal velocity scale when ground heating or cooling occurs. DDA further argues that a local characteristic vertical velocity having dimensions L_z/t_c, but encoding buoyancy sources, can also be defined using $w_* = \left(\beta \overline{w'T'} z\right)^{1/3}$ for the ASL. With these arguments, DDA proposes a new horizontal velocity that must be formed from L_x/t_c and a logical choice would be a $u_{**} = u_*^2/w_*$ provided $w_* \neq 0$. Likewise, the ASL temperature scale T_* must be replaced by $T_{**} = \overline{w'T'}/w_*$. The ensuing analysis proposes that the ASL be decomposed into 3 sublayers: dynamic (or near-neutral with $w_* = 0$ and already discussed), dynamic-convective, and free convective (Kader & Yaglom, 1990) with $w_* \neq 0$. Hence, for the dynamic convective case, DDA argues that

$$\frac{\overline{u'\theta'_v}}{u_{**}T_{**}} = \frac{w_*^2}{u_*^2}\frac{\overline{u'\theta'_v}}{\overline{w'\theta'_v}} = \text{constant}.$$

Thus, DDA predicts that

$$R_h = -\frac{\overline{u'\theta'_v}}{\overline{w'\theta'_v}} = \text{constant} \times \frac{u_*^2}{w_*^2} = \text{constant} \times \frac{u_*^2}{\left(\beta\overline{w'T'}z\right)^{2/3}} = \text{constant} \times \kappa^{2/3}\zeta^{-2/3}.$$

This DDA prediction was already confirmed using multiple data sources (Kader & Yaglom, 1990). Figure 1 illustrates the comparison between MOST and DDA predictions for $\phi_m(\zeta)$ and $\phi_h(\zeta)$ in panel (a), $\phi_\varepsilon(\zeta)$ in panel (b), and the resulting $R_h(\zeta)$ in panel (c). The two frameworks agree well in near-neutral conditions but diverge substantially in the unstable regime.

2.2.4 A Dougherty-Ozmidov Scaling for Stably Stratified Flows

For near neutral to slightly stable conditions, it may be argued that MOST applies and the usual corrections can be used in the longitudinal heat flux budgets. However, as the effects of stable stratification increase (e.g. $|\zeta| > 0.2$), L_o is no longer the most appropriate length scale characterizing the effects of stratification on eddy sizes. Instead, the Dougherty-Ozmidov scale L_{DO} may be the relevant length because it is the size of the largest eddy unaffected by buoyancy (Dougherty, 1961; Grachev et al., 2015; Li et al., 2016). Thus, when $z/L_{DO} \ll 1$, MOST scaling applies. However, when $z/L_{DO} > 1$, the Dougherty-Ozmidov scaling variables may be more relevant. The appropriate length, velocity, and temperature normalizing variables associated with the Dougherty-Ozmidov scaling are (Li et al., 2016; Grachev et al., 2015):

$$L_{DO} = \left(\frac{\varepsilon}{N_{BV}^3}\right)^{1/2}; U_{DO} = \left(\frac{\varepsilon}{N_{BV}}\right)^{1/2}; \theta_{DO} = \frac{\sqrt{\varepsilon N_{BV}}}{\beta}; N_{BV} = \sqrt{\beta \Gamma_\theta},$$

where N_{BV} is the Brunt-Vaisala frequency. Thus, it may be anticipated that for stable stratification,

$$\frac{\overline{u'\theta_v'}}{U_{DO}\ \theta_{DO}} = \phi_{u\theta}(\zeta).$$

2.3 The Longitudinal Heat Flux Co-Spectrum

Moving from RANS analysis to co-spectral analysis, the shape of the longitudinal heat flux co-spectrum $F_{u\theta}(k_x)$ with k_x is now considered. The co-spectrum satisfies the normalizing property

$$\frac{\int_0^\infty F_{u\theta}(k_x) dk_x}{\overline{u'\theta_v'}} = 1. \tag{21}$$

2.3.1 Dimensional Analysis for the Inertial Subrange: A Review

For the ISR, the possible list of variables to be included are as follows (Tennekes & Lumley, 1972):

- Eddy sizes or wavenumbers: k_x,
- Standard ISR variables in 'conservative' cascades that include ε and temperature variance dissipation rate ε_θ. They are relevant when the transfer of TKE and $\overline{\theta_v'^2}$ across scales or k_x are dissipated by molecular processes (i.e. kinematic viscosity and thermal diffusivity),
- External mean flow effects that act on all k_x in the generation mechanism: $\Gamma = \partial\overline{U}/\partial z$ and $\Gamma_\theta = \partial\overline{\theta_v}/\partial z$.

With this list and upon defining length [L], time [T], and temperature [K] as basic dimensions, it is straightforward to show that (Cava & Katul, 2012; Mortarini et al., 2025)

$$F_{u\theta}(k_x) = k_x^a \varepsilon^b \varepsilon_\theta^c \Gamma^d \Gamma_\theta^e; \quad \frac{[L]^2[K]}{[T]} = \left(\frac{1}{[L]}\right)^a \left(\frac{[L]^2}{[T]^3}\right)^b \left(\frac{[K]^2}{[T]}\right)^c \left(\frac{1}{[T]}\right)^d \left(\frac{[K]}{[L]}\right)^e, \tag{22}$$

leading to the following dimensional constraints:

$$[K] : 1 = 2c + e \tag{23}$$
$$[T] : 1 = 3b + c + d \tag{24}$$
$$[L] : 2 = -a + 2b - c. \tag{25}$$

That is, five variables and 3 dimensions are available and the problem is indeterminate. However, limiting cases can still be derived and are summarized below:

- When $F_{u\theta}(k_x)$ is assumed to vary with k_x, ε and ε_θ (i.e. no mean gradients or production variables), dimensional analysis requires that $F_{u\theta}(k_x) \sim \varepsilon_\theta^{1/2}\varepsilon^{1/6}k_x^{-5/3}$. This scaling is compatible with the constant correlation coefficient later described.
- When $F_{u\theta}(k_x)$ is assumed to vary with k_x and mean gradient quantities only (i.e. Γ and Γ_θ – and thus dominated by production terms), then $F_{u\theta}(k_x) \sim (\Gamma)(\Gamma_\theta)k_x^{-3}$.
- When $F_{u\theta}(k_x)$ is assumed to vary with k_x, ε_θ and Γ (i.e. mixed quantities), then $F_{u\theta}(k_x) \sim (\Gamma\varepsilon_\theta)^{1/2}k_x^{-2}$.
- When $F_{u\theta}(k_x)$ is assumed to vary with $k_x^{-5/2}$ (reported in several studies), ε_θ, Γ, and Γ_θ, then $F_{u\theta}(k_x) \sim (\Gamma\varepsilon_\theta)^{1/2}\Gamma_\theta^{-1}k_x^{-5/2}$.
- When $F_{u\theta}(k_x)$ is assumed to vary with k_x, ε and Γ_θ (another mixed quantity), then $F_{u\theta}(k_x) \sim \Gamma_\theta\varepsilon^{1/3}k_x^{-7/3}$.

These results cover the entire range of scaling exponents already reported in the literature for the ISR. When combined with the analysis of the RANS budget, the following conjectures can be made: In the asymptotic near-convective and near-neutral limits, the terms associated with P_m are not significant and $k_x^{-5/3}$ is expected to hold for the ISR. For the dynamic convective limit, where Γ and Γ_θ are large, mixed scaling is likely to dominate (i.e. $k_x^{-6/3}$ to $k_x^{-7/3}$). For mildly stable conditions, a $k_x^{-5/2}$ was also confirmed (Caughey, 1977).

One more prediction in the ISR was offered from the Eddy-Damped Quasi Normal Model (EDQNM). In this analysis, ε_θ was excluded and it directly follows from the reduced dimensional considerations here (i.e. $c = 0$) that the co-spectrum is given by (W. J. Bos & Bertoglio, 2007)

$$F_{u\theta}(k_x) \sim \Gamma_\theta\Gamma^d\varepsilon^{(1-d)/3}k_x^{-(7+2d)/3}, \tag{26}$$

where $d = 1/3$ was determined using DNS. With such a d, Equation 26 becomes

$$F_{u\theta}(k_x) \sim \Gamma_\theta\Gamma^{1/3}\varepsilon^{2/9}k_x^{-23/9}. \tag{27}$$

The exponent $23/9 = 2.55$ is close to what was reported for some field experiments (Kaimal et al., 1972) where an exponent $= 5/2$ was empirically determined.

2.3.2 Dimensional Analysis for Large Eddies

In a near-neutral limit for scales much larger than z but much smaller than δ, it is anticipated that both z and δ are no longer relevant length scales. Thus, a plausible choice for the normalizing variables of the co-spectrum are u_* and T_* so that

$$F_{u\theta}(k_x) = C_1 u_* T_* k_x^{-1} = C_1 \left(\overline{w'\theta'_v}\right) k_x^{-1}. \tag{28}$$

The k_x^{-1} scaling has received experimental support (Kader & Yaglom, 1991) for the dynamic sublayer and the free convective limit with $C_1 = -0.6$ for the dynamic sublayer and $C_1 = -0.14$ for the free convective limit, although the study did not formalize this as a general scaling law, noting the increased sensitivity of scalar–velocity cospectra to anisotropy and stratification. In mildly stable stratification, it was reported that $F_{u\theta}(k_x)$ scales as k_x^{-1} up to low frequencies commensurate to $N_{BV} = \sqrt{\beta\Gamma_\theta}$ (Caughey, 1977).

The scaling for large eddies and mildly stable conditions can be derived from normalizing by $N_{BV} = \sqrt{\beta\Gamma_\theta}$ and β, such that

$$F_{u\theta}(k_x) = \frac{1}{\beta}N_{BV}^3 k_x^{-3} \tag{29}$$

Interestingly, for frequencies much smaller than N_{BV}, an approximate k_x^{-3} scaling may be a plausible description for the data in the aforementioned study (Caughey, 1977). This scaling is consistent with Γ and Γ_θ being the only dynamically relevant variables describing very large scales (i.e. those commensurate with mean-flow variables).

2.3.3 The Constant Scalewise Correlation Hypothesis

One field study reports a constant scale-wise correlation coefficient defined as (Antonia & Zhu, 1994)

$$\frac{F_{u\theta}(k_x)}{F_{uu}(k_x)^{1/2}F_{\theta\theta}(k_x)^{1/2}} = \text{constant}. \tag{30}$$

This constant correlation appeared to extend to scales larger than those associated with the ISR. For ISR scales, setting $F_{uu}(k_x) = C_o\varepsilon^{2/3}k_x^{-5/3}$ and $F_{\theta\theta}(k_x) = C_T\varepsilon_\theta\varepsilon^{-1/3}k_x^{-5/3}$, the constant correlation coefficient argument would lead to

$$F_{u\theta}(k_x) = \sqrt{C_TC_o}\varepsilon^{1/6}\varepsilon_\theta^{1/2}k_x^{-5/3}, \tag{31}$$

where $C_o = 0.55$ is the Kolmogorov constant and $C_T = 0.8$ is the Kolmogorov-Obukhov-Corrsin constant (Kaimal & Finnigan, 1994; Hsieh & Katul, 1997).

This is the expected outcome when Γ and Γ_θ are not introduced as dynamically relevant, which is equivalent to assuming that the generation mechanism is weak and only energy transfer across scales is relevant. To what degree this constant-correlation hypothesis holds across stability regimes, heights from the grounds, and scales larger than the ISR have not been fully explored and motivate the analysis here.

2.3.4 A Co-Spectral Budget (CSB): General Considerations

A scale-by-scale budget for $F_{u\theta}(k_x)$, hereafter referred to as the co-spectral budget (CSB), mirroring the terms in the stationary RANS model may be written as

$$\frac{\partial}{\partial t}F_{u\theta}(k_x) = 0 = P_{u\theta}(k_x) + T_{u\theta}(k_x) + \pi_{u\theta}(k_x) - (\nu + D_m)k_x^2F_{u\theta}(k_x), \tag{32}$$

where $P_{u\theta}(k_x)$ is the scale-wise production (mirroring P_m), $T_{u\theta}(k_x)$ is the scale-wise heat flux transfer (mirroring the flux transport), $\pi_{u\theta}(k_x)$ is the pressure de-correlation term, and the last term are the molecular terms decorrelating u' from θ_v' at scale k_x. Those molecular terms are expected to be significant at scales commensurate to the Kolmogorov micro-scales. The $P_{u\theta}(k_x)$ is given by

$$P_{u\theta}(k_x) = F_{wu}(k_x)\ \Gamma_\theta(z) + F_{w\theta}(k_x)\ \Gamma(z), \tag{33}$$

where $F_{uw}(k_x)$ and $F_{w\theta}(k_x)$ are the momentum and sensible heat flux co-spectra, respectively. The influence of thermal heterogeneity on $F_{u\theta}(k_x)$ primarily enters through this production term, which depends explicitly on $F_{uw}(k_x)$ and $F_{w\theta}(k_x)$. In particular, $F_{w\theta}(k_x)$ represents the vertical heat flux and therefore carries the spectral signatures associated with temperature variance and heterogeneity. The pressure de-correlation may be modeled using a spectral Rotta scheme, which represents the wavenumber-by-wavenumber analogue of the Rotta closure employed for the bulk heat-flux budget (i.e. Equation 4), given as (Besnard et al., 1996; G. G. Katul et al., 2014; Li, 2019)

$$\pi_{u\theta}(k_x) = -\frac{C_R}{\tau_d(k_x)}F_{u\theta}(k_x) - C_IP_{u\theta}(k_x), \tag{34}$$

where $\tau_d(k_x)$ is a scale-dependent relaxation time presumed to vary with ε and k_x. For the inertial subrange, $\tau_d(k_x) = \varepsilon^{-1/3}k_x^{-2/3}$ but for eddy sizes much larger than their inertial subrange counterparts, $\tau_d(k_x) = \varepsilon^{-1/3}k_a^{-2/3}$, where k_a is an inverse of a macro-scale eddy size L_p (e.g. $\sim 1/L_p$). Much like the flux transport term in RANS, the flux transfer term across scales also requires a spectral closure model. A typical closure scheme assumes that the longitudinal heat flux occurs 'down-scale' by diffusion and is given by

$$T_{u\theta}(k_x) = -\frac{\partial}{\partial k_x}\left[\frac{A_{u\theta}k_x}{\tau_d(k_x)}F_{u\theta}(k_x)\right], \tag{35}$$

where $A_{u\theta}$ is a similarity coefficient. This closure model assumes that the scale-wise flux transfer is only driven by local interactions and any non-local transfer must be either small or is accommodated by a non-universal $A_{u\theta}$. Using this spectral closure scheme, the overall flux transport term in RANS, represented by the scale-wise integrated flux transfer term here, remains negligible because

$$\int_0^\infty T_{u\theta}(k_x)dk_x = -A_{u\theta}\left[\frac{k_x}{\tau_d(k_x)}F_{u\theta}(k_x)\right]_{k_x=0}^{k_x=\infty} = 0. \tag{36}$$

Equation 36 is satisfied when $F_{u\theta}(k_x) \to 0$ faster than $[k_x/\tau_d(k_x)] \to \infty$ as $k_x \to \infty$. This condition is ensured because ignoring the molecular destruction terms necessitates that $k_x^2 F_{u\theta} \to 0$ as $k_x \to \infty$. To summarize, $T_{u\theta}(k_x)$ need not be zero at every k_x even when the flux transport term is ignored in a RANS analysis.

Under the assumption that pressure-transport terms are negligible — consistent with standard RANS closure modeling — a locally equilibrated CSB whereby the scale-by-scale balance is between production and pressure-redistribution yields

$$F_{u\theta}(k_x) = -\frac{1-C_I}{C_R}\tau_d(k_x)\left[F_{wu}(k_x)\;\Gamma_\theta(z) + F_{w\theta}(k_x)\;\Gamma(z)\right]. \tag{37}$$

In this case, the molecular terms are ignored and $A_{u\theta}$=0.

In what follows, the CSB is discussed separately for large-scales and inertial subrange scales given the different representation for $\tau_d(k_x)$ in these two regimes.

2.3.5 The CSB in the Inertial Subrange

When the transfer and molecular terms are ignored thereby reducing the CSB to a balance between $P_{u\theta}(k_x)$ and $\pi_{u\theta}(k_x)$, Equation 37 predicts that $F_{u\theta}(k_x)$ scales as $k_x^{-7/3}$ when both $F_{uw}(k_x)$ and $F_{w\theta}(k_x)$ scale as $k_x^{-7/3}$ in the inertial subrange. However, this prediction alone does not explain the range of cospectral exponents reported in the literature. To investigate this discrepancy, we examine how retaining the transfer term modifies the predicted scaling. Retaining the transfer term, ignoring the molecular terms, and setting $\tau_d = \varepsilon^{-1/3}k_x^{-2/3}$ results in

$$\frac{\partial F_{u\theta}(k_x)}{\partial k_x} + \left[\frac{5}{3} + \frac{C_R}{A_{u\theta}}\right]\frac{F_{u\theta}(k_x)}{k_x} = \left(\frac{1-C_I}{A_{u\theta}\;\varepsilon^{1/3}}\right)\left[F_{uw}(k_x)\Gamma_\theta + F_{w\theta}(k_x)\Gamma\right]k_x^{-5/3}. \tag{38}$$

As with the RANS model, it is instructive to ask what is the limiting behavior of $F_{u\theta}(k_x)$ when $P_{u\theta}(k_x) \to 0$. Mathematically, this limit sets the homogeneous solution of Equation 38, while $P_{u\theta}(k_x)$ dictates the particular solution. The sum of these two solutions, homogeneous and particular, set the general solution for the co-spectral budget model in the inertial subrange. The homogeneous solution is given by

$$F_{u\theta}(k_x) = C_h k_x^{-5/3-(C_R/A_{u\theta})}, \tag{39}$$

where C_h is an integration constant that is related to a finite $\overline{u'\theta'_v}$ introduced at some scale that is then transferred to finer scales and dissipated by the pressure de-correlation term. The homogeneous solution is suggestive that deviations from a $F_{u\theta}(k_x) \sim k_x^{-5/3}$ scaling is linked to a finite $A_{u\theta}$. With a $C_R = 1.8$ and an $A_{u\theta} = 2.7$, the $F_{u\theta}(k_x) \sim k_x^{-7/3}$ is recovered. Likewise, an $F_{u\theta}(k_x) \sim k_x^{-5/2}$ and an $F_{u\theta}(k_x) \sim k_x^{-23/9}$ are recovered when setting, respectively, $A_{u\theta} = 2.16$ and $A_{u\theta} = 2.025$. Thus, a non-universal exponent for $F_{u\theta}(k_x)$ in the ISR may depend on the significance of the flux-transfer term. To solve Equation 38, $F_{uw}(k_x)$ and $F_{w\theta}(k_x)$ must be known or externally supplied. Upon imposing canonical shapes for these two co-spectra as derived from a reference height in the ASL well above the ground, contributions of the $P_{u\theta}(k_x)$ on the longitudinal heat flux co-spectrum can be explored directly using Equation 37 and indirectly using Equation 38. It is to be noted that when $P_{u\theta}(k_x) = A_p k_x^{-\beta_p}$ (i.e. a power-law), the general

solution may be expressed as

$$F_{u\theta}(k_x) = \underbrace{C_h k_x^{-5/3-(C_R/A_{u\theta})}}_{Homogeneous} + \underbrace{\left(\frac{1-C_I}{A_{u\theta}\varepsilon^{1/3}}\right)\frac{A_p}{1-\beta_p+(C_R/A_{u\theta})}k_x^{-2/3-\beta_p}}_{Particular}. \quad (40)$$

Distortions from the $P_{u\theta}(k_x)$ to the inertial subrange of $F_{u\theta}(k_x)$ can thus be traced through the value of β_p across different stability regimes. Also dynamically interesting is the value of $A_{u\theta}$. As $A_{u\theta}$ increases and becomes much larger than $C_R(=1.8)$, the $F_{u\theta}(k_x)$ becomes dominated by the homogeneous solution that trends towards $k_x^{-5/3}$. Conversely, when $A_{u\theta}$ decreases, the homogeneous solution decays with increasing k_x rapidly and the particular solution (i.e. $-2/3-\beta_p$) dominates the scaling exponent of $F_{u\theta}(k_x)$. Thus, the scaling laws describing $F_{u\theta}(k_x)$ depend on two quantities that need not be universal: $A_{u\theta}$ (arising from the flux transfer contribution) and β_p (arising from the production contribution to the inertial subrange). This finding alone may explain why no consistent inertial subrange exponent was reported in the literature for $F_{u\theta}(k_x)$.

2.3.6 The CSB for the Large Scales

As before, retaining the transfer term, ignoring the molecular terms, and setting $\tau_d = \varepsilon^{-1/3}k_a^{-2/3}$ results in a revised model given by

$$\frac{\partial F_{u\theta}(k_x)}{\partial k_x} + \left[1+\frac{C_R}{A_{u\theta}}\right]\frac{F_{u\theta}(k_x)}{k_x} = \left(\frac{1-C_I}{A_{u\theta}\ \varepsilon^{1/3}k_a^{2/3}}\right)\left[F_{uw}(k_x)\Gamma_\theta + F_{w\theta}(k_x)\Gamma\right]k_x^{-1}. \quad (41)$$

Upon setting $P_{u\theta}(k_x) = A'_p k_x^{-\beta'_p}$ (coefficients can differ from their inertial subrange), the general solution is

$$F_{u\theta}(k_x) = \underbrace{C_h k_x^{-1-(C_R/A_{u\theta})}}_{Homogeneous} + \underbrace{\left(\frac{1-C_I}{A_{u\theta}\varepsilon^{1/3}k_a^{2/3}}\right)\frac{A'_p}{1-\beta'_p+(C_R/A_{u\theta})}k_x^{-\beta'_p}}_{Particular}. \quad (42)$$

Once again, as $A_{u\theta}$ increases and becomes much larger than $C_R(=1.8)$, the $F_{u\theta}(k_x)$ becomes dominated by the homogeneous solution that trends towards k_x^{-1}. Conversely, when $A_{u\theta}$ decreases, the homogeneous solution decays with increasing k_x rapidly and the particular solution (i.e. $-\beta'_p$) dominates the scaling exponent of $F_{u\theta}(k_x)$. Thus, the scaling laws describing $F_{u\theta}(k_x)$ at large scales also depend on the same two quantities that need not be universal: $A_{u\theta}$ (arising from the flux transfer contribution) and β'_p (arising from the production contribution at large scales).

3 Experiments

Two ASL experiments described elsewhere (G. Katul et al., 1997; Huang, Brunner, et al., 2021; Huang et al., 2023) were used to assess the findings of the models. The main experiment involved a triaxial sonic anemometer measuring u', v', w' and θ'_v at $z =$ 2 m, complemented by a vertical array of 5 heights measuring both u' and θ'_v near the ground (0.06−1 m) over a uniform and flat site. The second experiment involved a single triaxial sonic anemometer positioned at $z = 5.2$ m above a large grass-covered forest clearing. This experiment is used to assess the robustness of the findings derived from the main experiment. Figure 2 shows the differences in surface cover and surroundings at these two sites.

3.1 SLTEST

The main experiment was conducted at the Surface Layer Turbulence and Environmental Science Test (SLTEST) facility in western Utah, USA, during the Idealized

horizontal Planar Array experiment for Quantifying Surface heterogeneity (IPAQS) in June 2018 (Morrison et al., 2021). Located in the Great Salt Lake Desert, the SLTEST site is characterized by low surface roughness (with long uninterrupted fetches in the dominant wind direction) and strong thermal heterogeneity (owing to salt patches on the surface created by variations in soil and salt deposits) (Metzger, 2002).

A triaxial sonic anemometer (Campbell Scientific CSAT3; 10 cm path length) recorded the three velocity components and virtual temperature at $z = 2$ m at 20 Hz from June 10–24, 2018, resulting in 720 30-min runs spanning strongly unstable to weakly stable conditions. For each run, a double coordinate rotation was applied to align the mean streamwise velocity with the x-axis and set $\overline{W} = 0$.

A nearby vertical array of miniature hot- and cold-wires located ≈20 m east of the sonic anemometer was used for profile measurements. The vertical array comprised five heights at $z = 0.0625, 0.125, 0.25, 0.5$, and 1.0 m, each instrumented with one Nano-Scale Thermal Anemometry Probe (NSTAP; 60 µm sensing length) and one temperature variant (T-NSTAP; 200 µm). Both probes were operated in constant-current anemometry and sampled at 100 Hz. The hot- and cold-wire sensors were separated by approximately 3.6 cm (corresponding to 2.54 cm offsets in both the vertical and horizontal directions) at each height. The motivation for this configuration was to develop a low-cost circuitry using entirely off-the-shelf components enabled by the nanoscale sensors' inherently high resolution and small thermal mass. Details about the nanoscale sensors and their in-house operating circuits based on a Wheatstone bridge without additional feedback circuitry can be found elsewhere (Huang, Brunner, et al., 2021; Huang & Katul, 2022).

For the vertical array, a three-day intensive operational period (18–20 June 2018) yielded nine 30-min records spanning slightly unstable (2), near-neutral (4), and slightly stable (3) conditions. Since the NSTAP array measures only the longitudinal velocity component and cannot be reoriented post-hoc, run selection was based on the sonic anemometer wind direction to ensure alignment with the mean flow (Huang, Katul, & Hultmark, 2021). This selection criterion accounts for the limited number of retained runs relative to the full dataset. Missing data in the subsequent analysis correspond to temperature sensor breakage at $z = 0.5$ m for all cases, and at $z = 0.0625$ m for the stable cases.

In this study, the sonic anemometer measurements are used to evaluate bulk statistics, as these are relatively insensitive to line-path averaging (Freire et al., 2019; Kaimal et al., 1968; Horst & Oncley, 2006) and benefit from a larger number of runs (see Fig. S1). Hot-wire measurements are used for cospectral analysis due to their higher spatial resolution. As shown in Figs. S2 and S3, both sensors agree at low wavenumbers, while the sonic spectra exhibit an earlier high-wavenumber roll-off, consistent with spatial averaging over the finite path length. The smaller footprint of the hot-wires also enables near-surface profile measurements, which are used to estimate gradients (Γ and Γ_θ). While the velocity and temperature measurements from this dataset have previously been used to validate the sensor platform (Huang, Brunner, et al., 2021), to examine clustering behavior (Huang, Katul, & Hultmark, 2021), and to assess logarithmic scaling in higher-order variances (Huang & Katul, 2022; Huang et al., 2023), the corresponding covariances are reported here for the first time.

3.2 The Duke Forest Grass Clearing

The three velocity components and virtual temperature were measured using a triaxial sonic anemometer between July 12 and 16, 1995, at z=5.2 m above a grass surface within a forest clearing at the Blackwood division of the Duke Forest near Durham, North Carolina. The forest clearing dimensions were 480 m by 305 m and the mast was situated at 250 m and 160 m from the north-end and west-end portions of a 10 m Loblolly pine forest edge respectively. The sampling frequency and sampling duration per run were 56 Hz and 19.5 min. The sonic anemometer (Gill Instruments/1012R2) path length was

Figure 2. Left: The 1-m vertical array of nano-scale sensors at the SLTEST site. Right: The Duke Forest Grass Clearing site.

0.149 m. The 5-day experiment provided 128 runs spanning slightly stable to dynamic-convective conditions. The site, experimental setup, and data processing are described elsewhere (G. Katul et al., 1997) and not repeated here.

3.3 Data Analysis

For all datasets, trends associated with varying freestream velocity were removed with a 5-min cutoff following Hutchins et al. (2012). Statistics were computed over each 30-min record for SLTEST and over each 19.5-min record for the Duke Forest grass clearing site. The same averaging windows are used consistently across all analyses, including Figures 4, 5, 6, and 7. Spectra and cospectra were estimated using Welch's method with 16 Hamming-windowed segments per record.

4 Results and Discussion

Findings from the RANS analysis are first presented followed by a discussion on the realizability constraints and estimates for the ratio R_h. Spectral and co-spectral outcomes are featured with a focus on the CSB model and its findings for inertial subrange and production scales. To convert time to wavenumbers, Taylor's frozen turbulence hypothesis (Taylor, 1938; Everard et al., 2021; Deshpande et al., 2023) is used without additional adjustments arising from finite turbulent intensities (J. Lumley, 1965; J. Wyngaard & Clifford, 1977; Hsieh & Katul, 1997).

4.1 Mean Longitudinal Heat Flux Profile

Median profiles of the correlation coefficient $R_{u\theta} = \overline{u'\theta'_v}/(\sigma_u \sigma_\theta)$ and the longitudinal heat flux $\overline{u'\theta'_v}$ for each stability class from the vertical array at SLTEST are presented in Fig. 3. Linear regression of the median profiles against $\log z$ yields regression coefficients indistinguishable from zero for all stability classes ($p > 0.05$), indicating that flux transport plays a negligible role in the longitudinal heat flux budget, with the dominant balance between production and pressure decorrelation (consistent with the RANS analysis presented in Section 2.1). Although the hot-wire dataset used here is limited to nine runs, which restricts statistical convergence, the trends shown in Fig. 3 are consistent across cases and align with theoretical expectations.

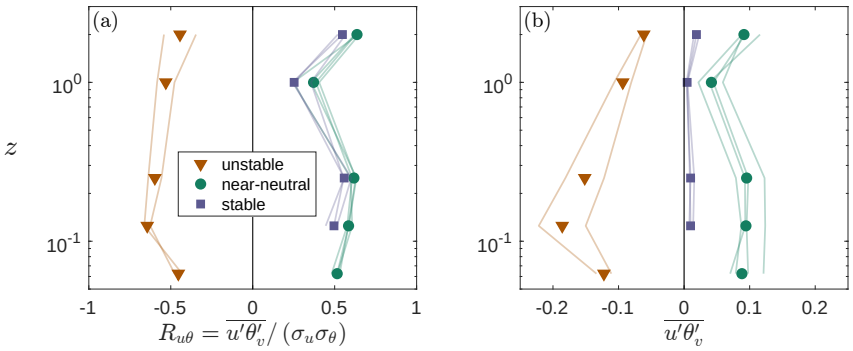

Figure 3. Profiles of $R_{u\theta} = \overline{u'\theta'_v}/(\sigma_u\sigma_\theta)$ (a) and of the longitudinal heat flux $\overline{u'\theta'_v}$ (b) at SLTEST, obtained from the vertical array for $z \leq 1$ m and the sonic anemometer at $z = 2$ m. Thin lines denote individual runs, while symbols indicate the median across runs within each stability class.

4.2 Thermal Stratification Effects on $R_{u\theta}$ and Its Realizability Constraint

Across the two sites, the $R_{u\theta}$ exhibit expected behavior across stability regimes (Fig. 4a), with $R_{u\theta} = 0$ at $\zeta = 0$ (where the absence of a mean temperature gradient eliminates systematic coupling between u' and θ'_v) and $R_{u\theta} \approx \pm 0.5$ for $|\zeta| > 0.01$ (reflecting the increasing correlation between velocity and temperature fluctuations as buoyancy forcing strengthens). The sign reversal across $\zeta = 0$ reflects the transition between upward transport of heat in unstable conditions and downward transport in stable conditions. The constraint $R_{u\theta} \leq +0.64$ for near-neutral to slightly unstable conditions (based on literature values of $R_{w\theta} = 0.5$ and $R_{uw} = -0.35$) bounds $R_{u\theta}$ for $|\zeta| < 0.05$. Moreover, all $|R_{u\theta}|$ values satisfy the realizability inequality (Equation 19). Fig. 4b also shows the attained fraction of the upper bound

$$\rho = \frac{|R_{u\theta}|}{|R_{uw}R_{w\theta}| + \sqrt{1 + R_{uw}^2 R_{w\theta}^2 - (R_{uw}^2 + R_{w\theta}^2)}} \in [0, 1]. \tag{43}$$

A $\rho = 1$ corresponds to an equality limit against stability. It can be seen that the equality limit is never reached, but near-neutral and stable conditions seem to reach about 0.6, while this fraction decreases with instability.

4.3 Thermal Stratification Effects on the Ratio R_h

As shown in Fig. 5a, both sites confirm that the ratio $R_h \approx 3$ for near-neutral conditions, with R_h decreasing rapidly as instability increases but approaching ≈ 4 under near-neutral and slightly stable conditions. These values are consistent with those reported in the literature (Kader & Yaglom, 1990), lending confidence in the reliability of the present dataset despite differences in site and instruments. For $|\zeta| < 0.05$ (near-neutral conditions), the small sensible heat flux leads to substantial scatter in the ratio R_h. Thus, Fig. 5b presents $\overline{u'\theta'_v}$ against $\overline{w'\theta'_v}$ for these conditions ($|\zeta| < 0.05$) only. With calculated SLTEST values of $\phi_m(0) = 1.09$, $\phi_h(0) = 0.57$, $\phi_\varepsilon(0) = 1.06$ (from the vertical array measurements at $z = 1$ m and averaged across the four near-neutral runs) and $\phi_{TKE}(0) = 6.48$ (from the sonic anemometer at $z = 2$ m, averaged across 68 $|\zeta| < 0.01$ runs), Equation 18 yields $R_h = 3.47$ in good agreement with measurements ($R_h = 3.62$). Here, gradients were obtained from logarithmic fits to the mean velocity and temperature profiles for each run. While $\phi_m(0)$, $\phi_\varepsilon(0)$, and $\phi_{TKE}(0)$ are close to expected neutral values, the reduced $\phi_h(0)$ suggests a departure from classical MOST behavior, potentially reflecting surface thermal heterogeneity and associated spatial variability in heat fluxes and temperature gradients. This is consistent with previous observations at

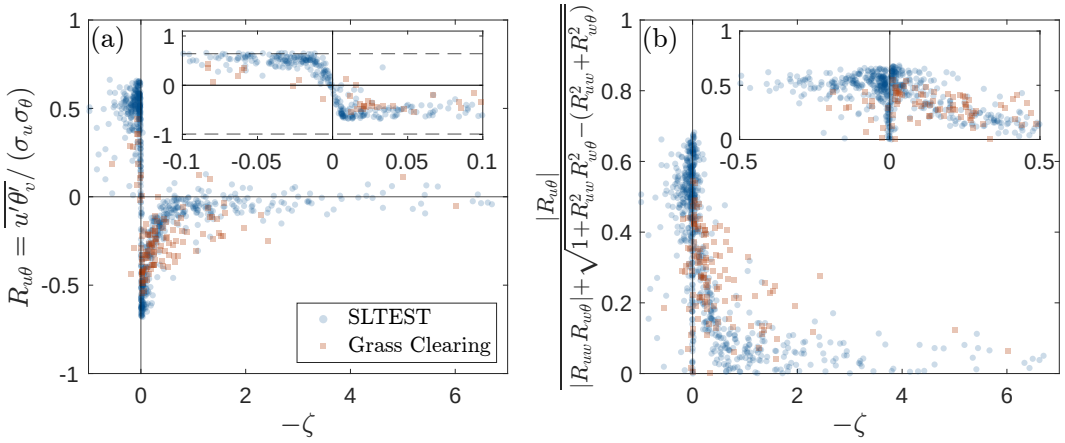

Figure 4. (a) Variations of the correlation coefficient $R_{u\theta}$ against stability for the SLTEST and the Duke Forest grass clearing datasets. Horizontal dashed lines represent the the realizability constraints $R_{u\theta} \in [-0.99, +0.64]$ based on values of $R_{w\theta} = 0.5$ and $R_{uw} = -0.35$. (b) Magnitudes of measured $R_{u\theta}$ normalized by the realizability constraint against stability.

SLTEST showing substantial spatial variability in heat fluxes and advective contributions arising from surface heterogeneity (Morrison et al., 2021). The $R_h = 3$ value based on expected MOST values at $\zeta = 0$ ($\phi_m(0) = 1$, $Pr_t(0) = 1$, $\phi_\varepsilon(0) = 1$, and $\phi_{TKE}(0) = 6.7$) is also shown for reference in Fig. 5a.

Figure 5c shows the ratio R_h normalized by u_*^2/w_*^2 based on DDA scaling, which exhibits better collapse than MOST-based scaling, particularly in the near-neutral region (for $|\zeta| < 0.05$, the interquartile range of the pooled near-neutral data decreases by approximately 70% under DDA normalization). Consistent with DDA predictions for dynamically convective conditions, $R_h/(u_*^2/w_*^2)$ approaches an approximately constant value as $-\zeta$ increases, with the median for $-\zeta > 0.25$ yileding a value of 0.74. The corresponding DDA prediction of $R_h \sim \zeta^{-2/3}$ is shown in Fig. 5d, where a near $-2/3$ power-law scaling in $|R_h|$ emerges as $-\zeta$ increases. Overall, the results suggest some cautionary support for DDA over MOST for the longitudinal heat flux scaling.

4.4 Dougherty-Ozmidov Scaling for Stably Stratified Flows

Normalization of $\overline{u'\theta'_v}$ with the Dougherty–Ozmidov scaling variables using both the SLTEST and the Duke Forest Grass clearing sonic datasets are shown in Fig. 5e. The normalized $\overline{u'\theta'_v}/U_{DO}\theta_{DO}$ tends towards a value of approximately 0.2 for $\zeta \gtrsim 0.1$, confirming that Dougherty–Ozmidov scaling captures the longitudinal heat flux under stable stratification. However, variability increases in the strongly stable regime, likely reflecting increased intermittency and the suppression of turbulence by buoyancy forces, which amplify the sensitivity of flux estimates to small-scale variability and noise. This increased variability could also suggests that shorter averaging windows than those used here (30 min for SLTEST and 19.5 min for the Duke Forest clearing) may be more appropriate under these conditions.

4.5 Spectral and Co-spectral Models

Relevant spectra and co-spectra of the two velocity components (u' and w') and the virtual temperature (θ'_v) from sonic anemometer data at both sites are shown in Figure 6 for near-neutral conditions ($|\zeta| < 0.05$, consistent with the cases presented in Fig-

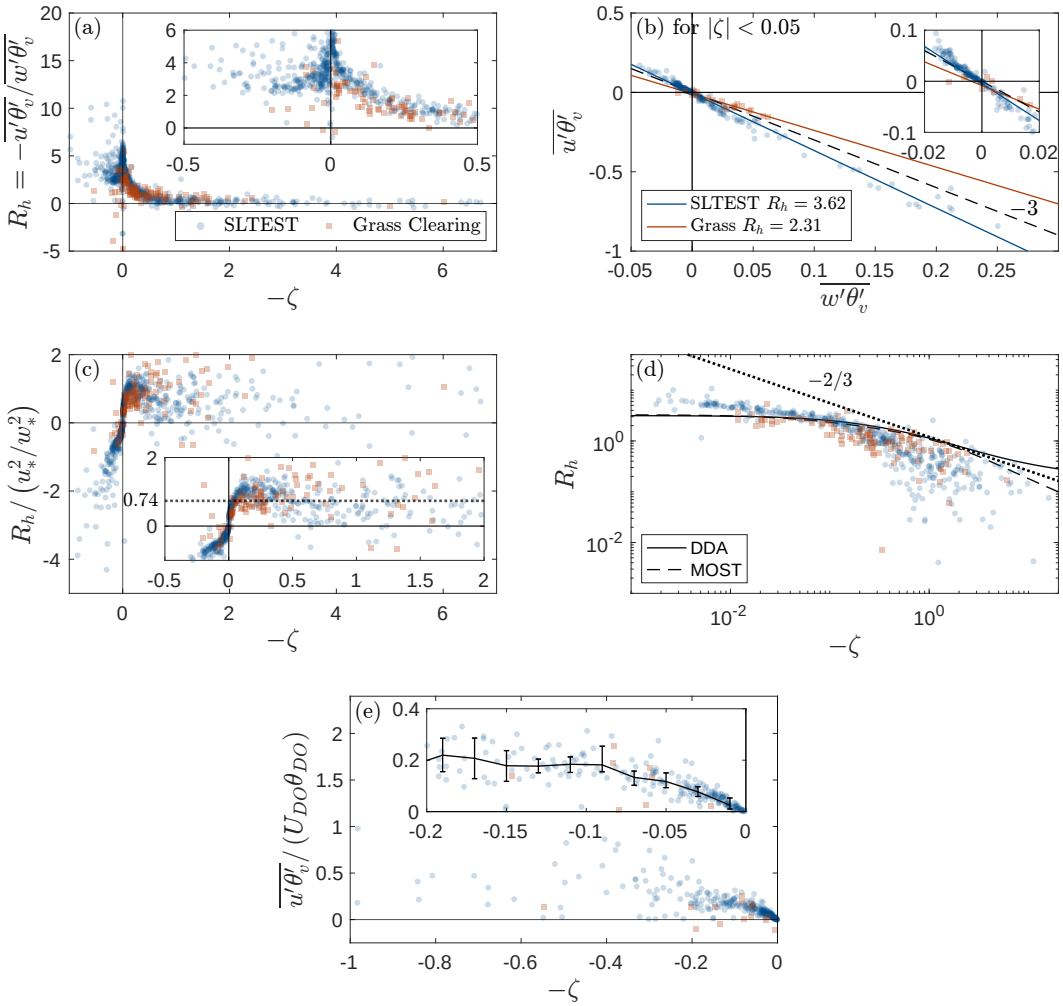

Figure 5. (a) Variations of the ratio R_h with the stability parameter ζ. (b) The relation between $\overline{u'\theta'_v}$ and $\overline{w'\theta'_v}$ for near-neutral conditions only ($|\zeta| < 0.05$). Lines of best fit for R_h are shown for both sites. (c) Variations of $R_h/(u_*^2/w_*^2)$ with the stability parameter ζ. DDA predicts $R_h/(u_*^2/w_*^2) \rightarrow$ constant. The dashed line indicates a constant value computed as the median for $-\zeta > 0.25$. (d) Variations of R_h with $-\zeta$, with the dashed line representing the predicted DDA scaling of $R_h \sim \zeta^{-2/3}$. (e) Variations of $\overline{u'\theta'_v}$ in Dougherty-Ozmidov scaling with stability under stable conditions ($-\zeta < 0$), where the scaling is expected to be valid. The inset shows bin-averaged medians pooled across both sites, with vertical bars spanning the interquartile range (25th–75th percentile).

ure 5b). In the inertial subrange at the grass site ($z = 5.2$ m), the spectra exhibit the expected $k_x^{-5/3}$ slope for $k_x z > 2$, and the co-spectra $F_{uw}(k_x)$, $F_{w\theta}(k_x)$, and $F_{u\theta}(k_x)$ display an approximate $k_x^{-7/3}$ scaling. Although the SLTEST dataset exhibit a similar tendency toward the expected slopes, the inertial subrange behavior is less distinct, likely because the sonic path length ($p \approx 10$ cm) attenuates fluctuations at wavenumbers $k_x > 1/p$ (Kaimal et al., 1968; Freire et al., 2019; Horst & Oncley, 2006), an effect that becomes more pronounced at lower measurement heights where the energetic eddy sizes are smaller. Spatial variability in surface heating at SLTEST– arising from the patchy distribution of salt deposits – may further contribute to the elevated noise observed in

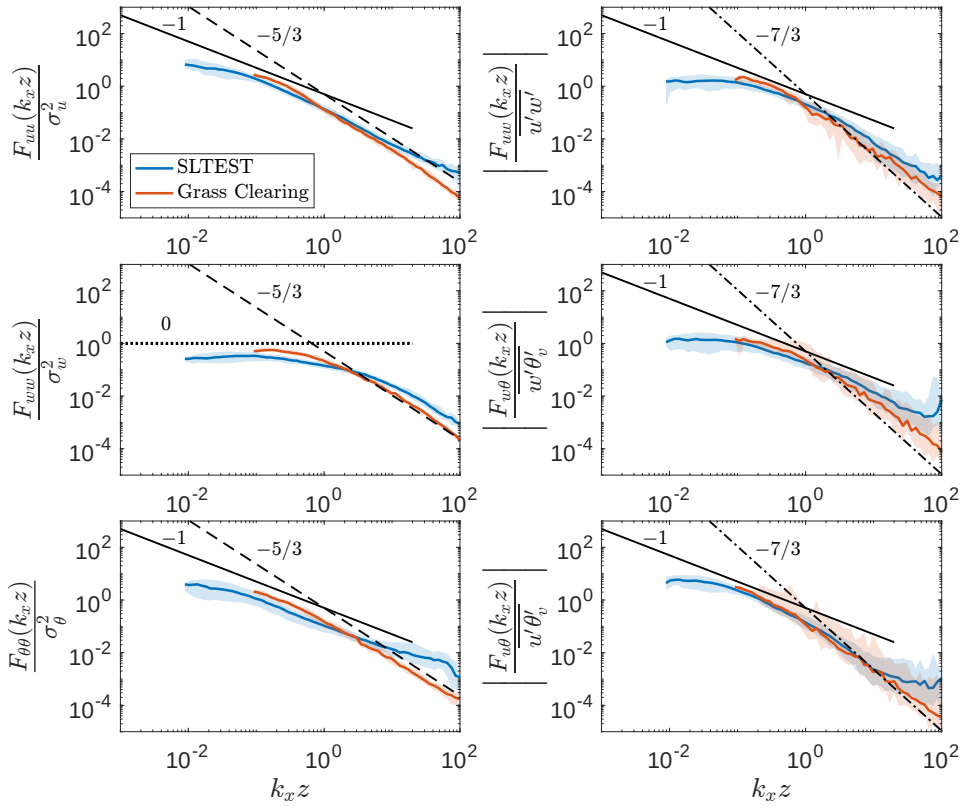

Figure 6. Dimensionless spectra (left column) and co-spectra (right column) under near-neutral conditions ($|\zeta| < 0.05$). The streamwise wavenumber k_x is normalized by the measurement height z. Solid colored lines indicate the ensemble median for SLTEST (blue) and the grass clearing (orange), while the shaded regions denote the 10–90% percentile range across realizations. Reference scaling laws are shown by dashed lines for the inertial-subrange spectral scaling $k_x^{-5/3}$ and dash-dotted lines for the co-spectral scaling $k_x^{-7/3}$. Solid black lines indicate the expected large-scale k_x^{-1} behavior for all spectra and co-spectra, except for $F_{ww}(k_x)$, where the dotted line denotes the expected k_x^0 scaling associated with wall-induced 'energy splashing' at large scales.

the co-spectra. At large scales (i.e. $k_x z < 0.5$), the spectra and co-spectra for both sites generally follow an approximate k_x^{-1} scaling, except for the vertical velocity spectra, which exhibits a k_x^0 region associated with energy splashing due to the randomizing effect of the ground on eddy impingement (Ayet et al., 2020; Hunt & Carlotti, 2001).

For the large scales of $F_{u\theta}$, both MOST and DDA normalization predict a k_x^{-1} dependence under near-neutral and unstable conditions. The corresponding proportionality constants from each framework, C_{MOST} and C_{DDA}, are shown in Fig. 7 for both sites. Near the neutral limit ($-\zeta < 0.5$), C_{MOST} increases sharply while C_{DDA} remains bounded, with mean values of 0.44 and 0.23 and corresponding coefficients of variation of 57% and 26%, respectively. As instability increases, both proportionality constants approach approximately steady values, though the scatter remains substantial for the current dataset (for $-\zeta > 0.5$, $C_{MOST} = 0.09 \pm 0.06$, $C_{DDA} = 0.23 \pm 0.14$). These results suggest that DDA yields a more consistent normalization of the large-scale longitudinal heat-flux cospectra, particularly under near-neutral conditions.

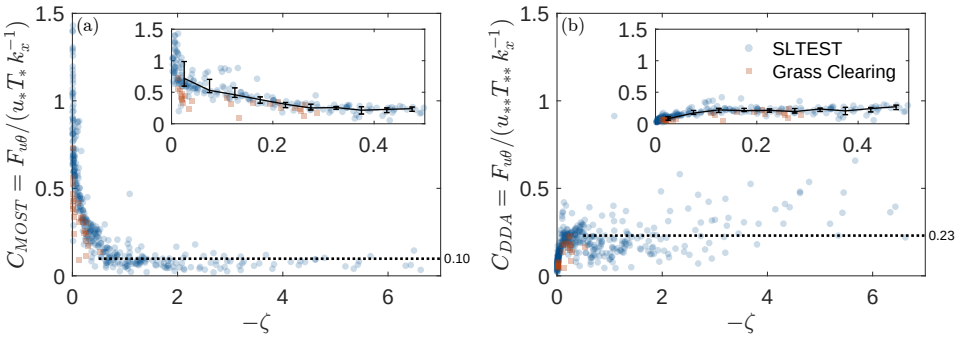

Figure 7. Fitted k_x^{-1} cospectral coefficients as a function of atmospheric stability for the MOST scaling (a) and the DDA scaling (b), where $F_{u\theta} = C_{MOST}\, u_* T_*\, k_x^{-1}$ and $F_{u\theta} = C_{DDA}\, u_{**} T_{**}\, k_x^{-1}$, respectively. Each point represents an individual run fitted over the large-eddy range where a k_x^{-1} slope is observed. Data are from SLTEST sonic anemometer measurements (blue), and the Duke Forest grass clearing sonic measurements (orange). Black lines and error bars in the insets denote the bin-median and interquartile range for bin sizes of 0.05.

Spectra and co-spectra of the horizontal velocity component (u') and virtual temperature (θ'_v) from the vertical array at SLTEST are shown for unstable, near-neutral, and stable conditions in Fig. 8. At large scales ($k_x z \in [1, 10]$), where the attached-eddy hypothesis is expected to hold, a k_x^{-1} scaling is evident across all stability regimes and for both the spectra and co-spectra.

For the inertial subrange, $F_{uu}(k_x)$ exhibits an approximate $k_x^{-5/3}$ scaling in all three stability cases. For $F_{\theta\theta}$, the $k_x^{-5/3}$ scaling is only apparent in the unstable condition. Under near-neutral and stable conditions, $F_{\theta\theta}$ exhibits limited inertial-subrange behavior and a more extended region of k_x^{-1} scaling. This finding is consistent with the enhanced logarithmic scaling of temperature variance (σ_θ) and higher-order moments discussed in Huang et al. (2023). In the cospectra $F_{u\theta}(k_x)$, the inertial subrange behavior seems to be approaching $k_x^{-7/3}$ for all stability cases although the slopes are shallower. At the lowest measurement height, $F_{u\theta}(k_x)$ exhibits a faster decay and a distinct dip around $k_x z \approx 1$, most pronounced under near-neutral and unstable conditions. This behavior likely reflects reduced coherence between velocity and temperature fluctuations in the immediate vicinity of the surface– where shear production dominates and buoyancy-driven structures are disrupted – as well as effects from probe separation, since the relative sensor spacing becomes significant at the smallest z. Excluding the lowest measurement height, the slopes m (where $F_{u\theta} \sim k_x^{-m}$) over the inertial subrange (defined for each run as $k_x > 10/L_u$ (where L_u is the integral length scale) and $f < 20$ Hz) are 1.90 ± 0.12, 1.67 ± 0.29, and 1.58 ± 0.26 for the unstable, near-neutral, and stable cases, respectively. This suggests that the near-neutral and stable cases, which are closer to $-5/3$ will yield a higher $A_{u\theta}$ (more contribution from the transfer term) in accordance with Equation 40.

Cospectral data from the vertical array at SLTEST are first used to evaluate the constant scale-wise correlation hypothesis (Fig. 9). In contrast to Antonia and Zhu (1994), where a constant $F_{u\theta}/\left(F_{uu}F_{\theta\theta}\right)^{1/2} \approx 0.1$ was observed within the inertial subrange, no such constant correlation is evident in the present dataset. The correlation coefficients within the inertial subrange roll off at height-dependent rates and onset scales, with earlier transitions generally occurring closer to the surface, and remain approximately constant only at large scales. At very high wavenumbers, the correlations flatten again at a scale corresponding roughly to the distance between the u' and θ'_v probes ($k_x d \approx 1$; Fig. 9 bottom row), as the sensors become spatially separated relative to the smallest eddies. The fact that the breakpoint does not occur exactly at $k_x d = 1$ could reflect

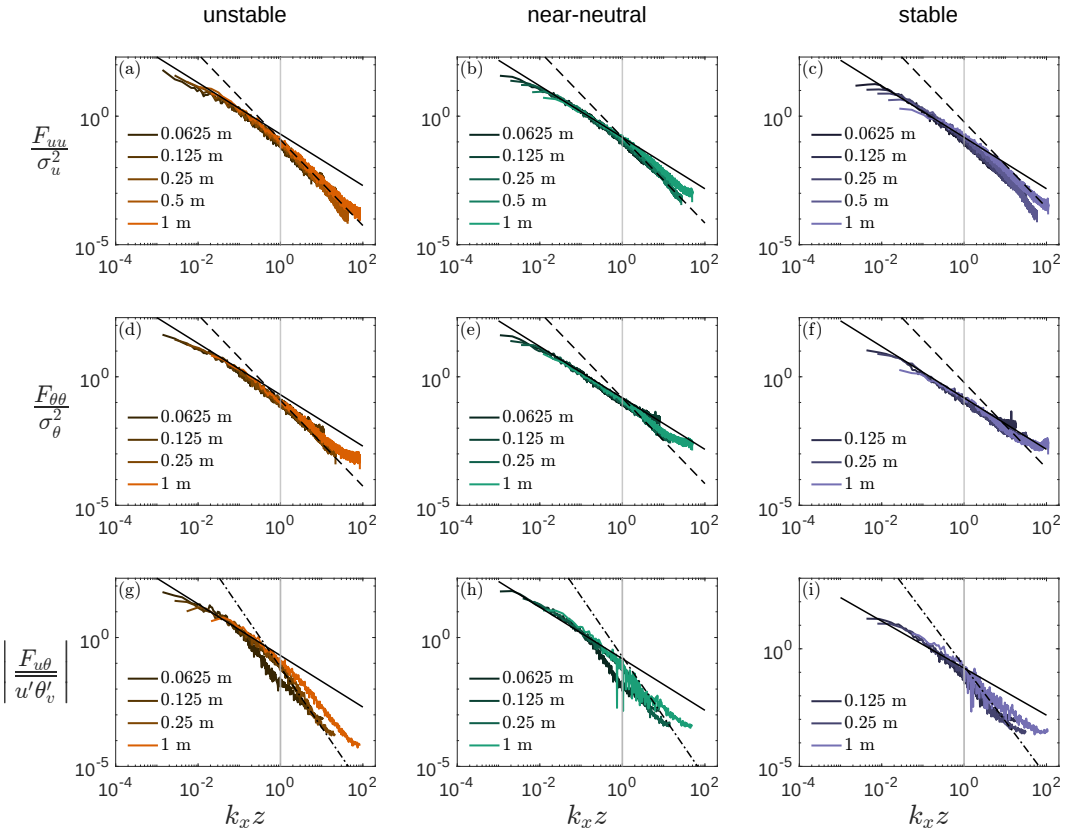

Figure 8. Dimensionless longitudinal velocity spectra (top row), temperature spectra (middle row), and co-spectra (bottom row) for unstable (left column), near-neutral (middle column), and stable (right column) conditions. The spectra and co-spectra shown are averages across multiple cases for each stability regime at each height (two unstable cases, four near-neutral cases, and three stable cases). The wavenumber k_x is normalized by z. The scaling exponents $k_x^{-5/3}$ (dashed line) for the spectra and $k_x^{-7/3}$ (dash-dot line) for the co-spectra are shown. The k_x^{-1} expected to hold for large scales is also presented for the spectra and cospectra (solid line).

random sweeping effects, where large-scale motions advect and distort the small-scale eddies, leading to additional decorrelation beyond that expected from geometry alone. Similar results are observed from the sonic anemometer data at both the SLTEST and grass sites under near-neutral conditions (not shown).

4.6 The Co-Spectral Budget

Solutions to the co-spectral budget are examined using the SLTEST data. The production terms $|F_{w\theta}\Gamma|$ and $|F_{uw}\Gamma_\theta|$ are first calculated, where the cospectra $F_{w\theta}$ and F_{uw} are computed from sonic anemometer measurements at $z = 2$ m, and the gradients Γ and Γ_θ are obtained from the vertical array by fitting logarithmic profiles of velocity and temperature with height. As an example, the production terms $|F_{w\theta}\Gamma(z)|$ and $|F_{uw}\Gamma_\theta(z)|$ at $z = 1$ m, as well as their sum, are shown for unstable, near-neutral, and stable conditions in Fig. 10(a)-(c). For both unstable and stable conditions, $|F_{uw}\Gamma_\theta|$ contributes more significantly to the production, whereas under near-neutral conditions it is negligible, with only slight contributions at large scales. This partitioning is physically con-

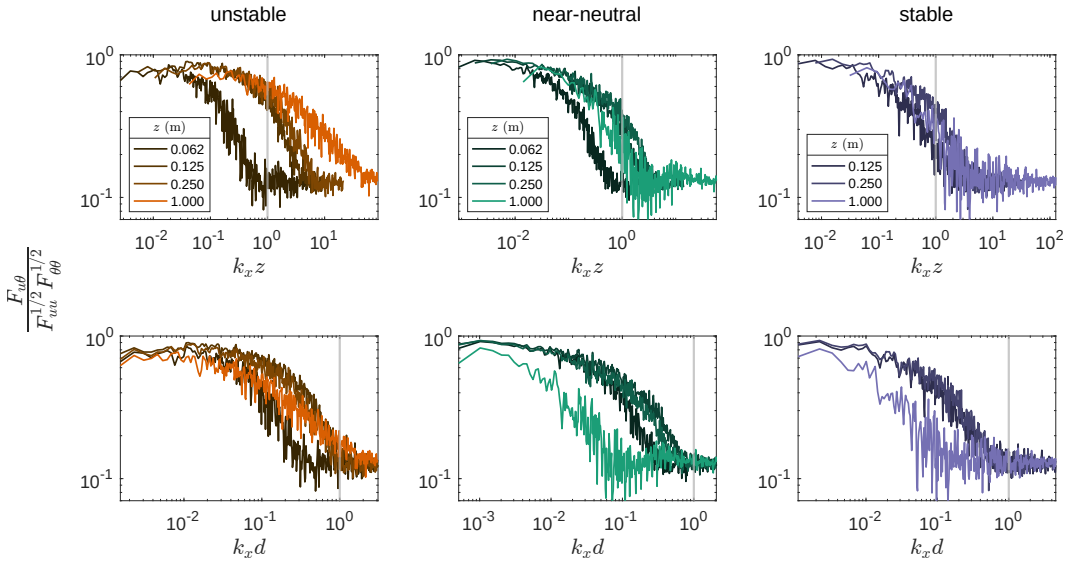

Figure 9. Top row: Scale-wise correlation $\rho(k_x)$ for slightly unstable (left), near-neutral (middle), and slightly stable (right) conditions at the SLTEST site. Bottom row: Same as top row but the wavenumber normalization is based on the separation distance d between θ_v' and u' measurements instead of z to emphasize the scales experiencing loss of covariance due to instrument configuration.

sistent, as the relative importance of each term reflects the balance between buoyancy and shear production across stability regimes.

To capture observed power-laws in $P_{u\theta}(k_x)$, a model function in the spirit of the von Kármán spectrum is fitted to the production term beyond the spectral maximum,

$$P_{u\theta}(k_x) = \frac{A}{k_x} \frac{1}{(1 + Bk_x^2)^{\gamma}}, \tag{44}$$

where A, B, and γ are constants determined from nonlinear regression. This formulation is selected because it reproduces the observed k_x^{-1} behavior for large scales (as $k_x \to 0$) and is not designed to capture the very large scales beyond this range. At small scales (large k_x), $P_{u\theta} \to AB^{-\gamma} k_x^{-1-2\gamma}$ such that $\gamma = 2/3$ corresponds to a $k_x^{-7/3}$ scaling. Best-fits for $P_{u\theta}$ are presented for the unstable, near-neutral, and stable cases at $z = 1$ m in Fig. 10(a)-(c). The near-neutral and unstable cases exhibit fitted exponents of $\gamma = 0.34$ and 0.51, corresponding to limiting high-wavenumber slopes of approximately $k_x^{-1.7}$ and $k_x^{-2.0}$, respectively. In contrast, the stable case displays a steep decay with $\gamma = 0.81$ and $P_{u\theta} \sim k_x^{-2.62}$, indicating that covariance generation is confined almost entirely to the large eddies with minor contributions from the inertial subrange.

To ensure continuity across the transition from large-eddy to inertial-subrange scales, the co-spectral budget ODEs (Eqs. 38 and 41) are unified using a smooth relaxation time

$$\tau_d(k_x) = \varepsilon^{-1/3} (k_x^n + k_a^n)^{-2/3n} \tag{45}$$

(with $n = 4$) that recovers the asymptotic forms $\tau_d = \varepsilon^{-1/3} k_a^{-2/3}$ for $k_x \ll k_a$ and $\tau_d = \varepsilon^{-1/3} k_x^{-2/3}$ for $k_x \gg k_a$. Figure 10(d)–(l) show the measured cospectra $|F_{u\theta}(k_x)|$ at $z = 0.125$, 0.25, and 1 m under unstable, near-neutral, and stable conditions together with their fitted CSB solutions. The height dependence of the fitted cospectra here arises through the production term, which depends on the local mean gradients $\Gamma(z)$ and $\Gamma_\theta(z)$.

The homogeneous (transfer-driven) and particular (production-driven) components of the solutions are also shown to evaluate their relative importance across scales and stability regimes.

The relative contributions of the homogeneous and particular solutions exhibit a clear dependence on wavenumber and height. In general, the particular solution is most significant at the large scales (low $k_x z$) and decays rapidly with increasing wavenumber, such that the small-scale behavior is dominated by the homogeneous component at all heights and across all stability. The contribution of the particular solution also diminishes with height, such that at $z = 1$ m, the cospectra are largely governed by the homogeneous solution across most of the wavenumber range. This decay with height becomes more rapid as stability increases.

These observations point to an increasing relative importance of spectral transfer with height and stability. This trend is consistent with the behavior of the transport coefficient $A_{u\theta}$, and is also reflected in the fitted cospectral ISR slopes, which decrease from approximately $m \approx 2.1$ under unstable conditions to $m \approx 1.6$ under stable conditions, approaching the classical $-5/3$ scaling as the relative importance of transport increases (Equation 40 as $A_{u\theta}$ becomes large). In general, the homogeneous solution remains important across all heights and stability conditions considered here, while the production-driven particular solution plays a significant role primarily near the surface.

The extent to which these results generalize across different flow conditions remains an open question due to the limited number of cases presented here. Nevertheless, the results demonstrate the utility of the CSB framework as a diagnostic tool for quantifying the relative contributions of production, transfer, and pressure decorrelation to cospectral structure. Importantly, the present results highlight a key limitation of Reynolds-averaged interpretations when applied to scale-dependent flux dynamics: while RANS-based arguments identify dominant terms in the mean budget, they neglect the role of transfer, and therefore cannot capture how flux is redistributed across scales or how the composite spectral structure arises.

5 Conclusions

This work examined the mean and co-spectral characteristics of the longitudinal heat flux through its Reynolds-averaged Navier-Stokes equations in the atmospheric surface layer. The scaling behaviors are evaluated using two experiments: (i) a nanoscale sensing platform within the first meter above the surface with a nearby sonic anemometer at $z = 2$ m over the Utah salt flats (SLTEST), and (ii) a conventional sonic anemometer deployed over a grass clearing in Duke Forest (North Carolina).

The Reynolds-averaged analysis showed that the vertical variation in the turbulent heat flux $\overline{u'\theta'_v}$ serves as a practical diagnostic for flux transport: when $\partial_z \overline{u'\theta'_v}$ is appreciable, the flux–transport term is non-negligible and comparable in magnitude to pressure–decorrelation; conversely, when $\overline{u'\theta'_v}$ shows little or no z-dependence, the flux–transport contribution is small and may be neglected. Accordingly, data at SLTEST showed that the profile of the longitudinal heat flux $\overline{u'\theta'_v}$ was nearly constant with height (no strong z-dependence), suggestion that the flux–transport contribution is small in a mean sense. Key non-dimensional quantities including the correlation coefficient $R_{u\theta}$ and the ratio between horizontal and vertical heat flux R_h were consistent with values reported in the literature for surface-layer turbulence. The data also adhered to realizability constraints: under stable stratification $|R_{u\theta}|$ attained about 0.6 of its theoretical upper limit, and this fraction decreased as atmospheric stability conditions became unstable. Directional Dimensional Analysis (DDA) produced an improved collapse in the ratio R_h across stability regimes relative to the standard Monin–Obukhov Similarity Theory (MOST), indicating that DDA captures additional directional and anisotropic effects relevant to near-

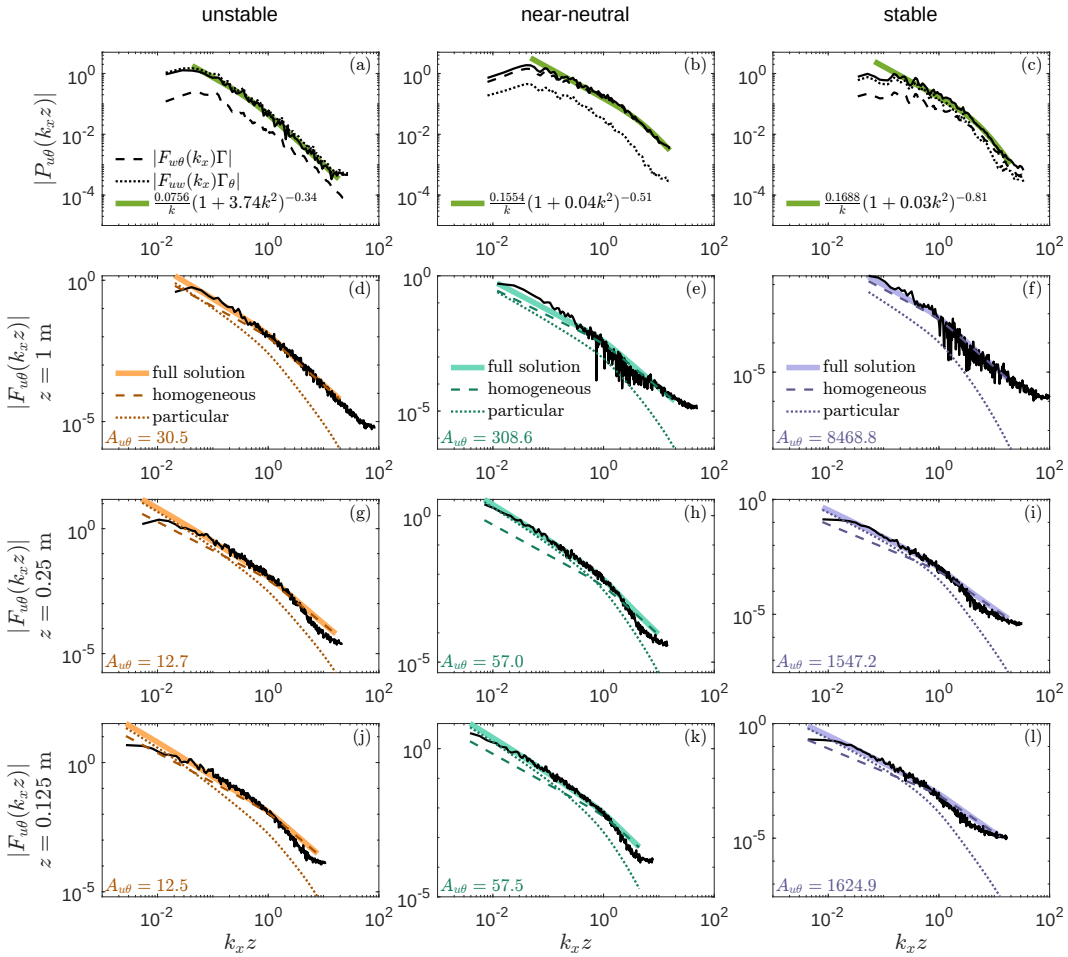

Figure 10. The two scale-wise production terms in the co-spectral budget and the regression fit to their sum when using Equation 44 for the unstable (a), near-neutral (b), and the stable (c) cases at $z = 1$ m. The remaining rows show the measured cospectra at $z = 1$, 0.25, and 0.125 m together with model predictions from the co-spectral budget (CSB) solution, along with the decomposed particular (production-driven) and homogeneous contributions.

surface turbulence. Both field sites, despite contrasting heterogeneity and measurement techniques, showed comparable trends and stability dependence, underscoring the robustness of the observed relations.

The cospectral analysis explored the scale-dependent behavior of the longitudinal turbulent heat flux. The assumption of constant scale-wise correlation held only for the largest eddies, with correlations decreasing systematically toward higher wavenumbers, in contrast to earlier findings (Antonia & Zhu, 1994) that reported a constant correlation extending in the inertial subrange wavenumbers.

The cospectral budget analysis revealed that the scaling in $F_{u\theta}(k_x)$ is dependent on two non-universal parameters: $A_{u\theta}$ from the flux transfer contribution and β_p from the production contribution. The parameter β_p is in turn dependent on two co-spectra, F_{uw} and $F_{w\theta}$, that contribute to production. In the large eddies where the attached eddy hypothesis is expected to hold, a robust -1 scaling in $F_{u\theta}(k_x)$ emerges since both F_{uw} and $F_{w\theta}$ exhibit approximate k^{-1} behavior. That is, since the production term $P_{u\theta}(k_x) =$

$F_{uw}(k_x)\Gamma_\theta + F_{w\theta}(k_x)\Gamma$ will likewise follow a k_x^{-1} dependence at the large scales, $F_{u\theta}(k_x)$ can inherit the same slope through the particular solution (β_p' in Equation 42). The homogeneous solution, governed by the relative strength of the flux-transfer coefficient $A_{u\theta}$, either matches this -1 scaling when $A_{u\theta}$ is large or becomes subdominant when $A_{u\theta}$ is small. Consequently, $F_{u\theta}(k_x)$ tends to display an overall k_x^{-1} dependence at large scales, consistent with observations and dimensional arguments from DDA, MOST, and Dougherty-Ozmidov scaling.

Within the inertial subrange, however, $F_{u\theta}(k_x)$ exhibits a large variability of cospectral slopes. Just as in the large eddy regime, how $F_{u\theta}(k_x)$ scales can be traced through the cospectral budget analysis to β_p, the production term scaling that in turn depends on the F_{uw} and $F_{w\theta}$ scaling, and the flux-transfer coefficient $A_{u\theta}$. However, unlike in the large eddies where F_{uw} and $F_{w\theta}$ both scale as k_x^{-1}, they tend to exhibit anomalous scaling in the inertial subrange, thus contributing to the wide range of scaling exponents reported in the literature. This framework reconciles long-standing discrepancies in reported inertial subrange exponents by explicitly linking deviations from universality to non-conserved flux transfer mechanisms unique to the longitudinal heat flux.

Further, decomposition of the cospectral budget into particular and homogeneous components allowed examination of the relative roles of production and flux-transfer in the cospectral evolution. SLTEST data showed that while the flux transport term appears insignificant in the mean balance, the flux transfer term plays a non-negligible role in its spectral counterpart across all scales and stability conditions. The particular solution (driven by the production term) was comparable to the homogeneous solution only close to the surface and rapidly falls off as z increases. For all stability cases, $A_{u\theta} > 7.7$ and suggests that flux-transfer is significant in the scale-to-scale evolution of the $F_{u\theta}(k_x)$. These results and observations are consistent with dimensional analysis for the inertial subrange, with Γ and Γ_θ entering the production term (and thus the particular solution), and ε setting the eddy relaxation time and ε_θ the scalar cascade rate (and thus the homogeneous solution).

Overall, the findings establish that the longitudinal turbulent heat flux, though often neglected in closure schemes, provides a new perspective into scale-dependent energy exchange and anisotropy in stratified turbulence. By elucidating when and how flux-transfer terms modulate spectral slopes, the results offer a pathway for improved parameterization of non-local transport in atmospheric models.

Conflict of Interest

The authors declare no conflicts of interest relevant to this study.

Open Research Section

The turbulence measurements analyzed in this study were obtained from the SLTEST facility and Duke Forest site. Data processing and analyses were conducted using MATLAB scripts. The code and processed datasets supporting the results are archived on atlas-uh (2026).

Acknowledgments

Measurements from SLTEST were supported by the U.S. National Science Foundation (AGS-1649067 and AGS-1649049). K.Y.H. and R.N. acknowledge support from start-up funds provided by the University of Houston. G.K. acknowledges support from the U.S. National Science Foundation (AGS-2028633) and the U.S. Department of Energy (DE-SC0022072). The authors declare no conflicts of interest.

References

Antonia, R., & Zhu, Y. (1994). Inertial range behaviour of the longitudinal heat flux cospectrum. *Boundary-Layer Meteorology*, *70*, 429–434.

Ayet, A., Katul, G., Bragg, A., & Redelsperger, J.-L. (2020). Scalewise return to isotropy in stratified boundary layer flows. *Journal of Geophysical Research: Atmospheres*, *125*(16), e2020JD032732.

atlas-uh (2026). atlas-uh/longitudinal_heat_flux_ASL: Version 1.0.0 [Dataset and Software]. Zenodo. `https://doi.org/10.5281/zenodo.19486142`

Besnard, D., Harlow, F., Rauenzahn, R., & Zemach, C. (1996). Spectral transport model for turbulence. *Theoretical and Computational Fluid Dynamics*, *8*(1), 1–35.

Betchov, R., & Yaglom, A. (1971). Notes on similitude theory for turbulence in an un-stably stratified fluid. *Izv. Akad. Nauk SSSR. Fizika Atmos. i Okeana*, *7*, 1270–1279.

Bink, N., & Meesters, A. (1997). Comment on 'estimation of surface heat and momentum fluxes using the flux-variance method above uniform and non-uniform terrain'by katul et al.(1995). *Boundary-Layer Meteorology*, *84*(3), 497–502.

Bos, W., Touil, H., Shao, L., & Bertogli, J. (2004). On the behavior of the velocity-scalar cross correlation spectrum in the inertial range. *Physics of Fluids*, *16*, 3818–3823.

Bos, W. J., & Bertoglio, J.-P. (2007). Inertial range scaling of scalar flux spectra in uniformly sheared turbulence. *Physics of Fluids*, *19*(2), 025104.

Bou-Zeid, E., Gao, X., Ansorge, C., & Katul, G. G. (2018). On the role of return to isotropy in wall-bounded turbulent flows with buoyancy. *Journal of Fluid Mechanics*, *856*, 61–78.

Bradley, E., Antonia, R., & Chambers, A. (1982). Streamwise heat flux budget in the atmospheric surface layer. *Boundary-Layer Meteorology*, *23*(1), 3–15.

Brugger, P., Katul, G., De Roo, F., Kröniger, K., Rotenberg, E., Rohatyn, S., & Mauder, M. (2018). Scalewise invariant analysis of the anisotropic reynolds stress tensor for atmospheric surface layer and canopy sublayer turbulent flows. *Physical Review Fluids*, *3*(5), 054608.

Canuto, V., Minotti, F., Ronchi, C., Ypma, R., & Zeman, O. (1994). Second-order closure pbl model with new third-order moments: Comparison with LES data. *Journal of Atmospheric Sciences*, *51*(12), 1605–1618.

Caughey, S. (1977). Boundary-layer turbulence spectra in stable conditions. *Boundary-Layer Meteorology*, *11*(1), 3–14.

Caughey, S., Wyngaard, J., & Kaimal, J. (1979). Turbulence in the evolving stable boundary layer. *Journal of Atmospheric Sciences*, *36*(6), 1041–1052.

Cava, D., & Katul, G. (2012). On the scaling laws of the velocity-scalar cospectra in the canopy sublayer above tall forests. *Boundary-Layer Meteorology*, *145*, 351–367.

Charuchittipan, D., & Wilson, J. (2009). Turbulent kinetic energy dissipation in the surface layer. *Boundary-Layer Meteorology*, *132*(2), 193–204.

Choi, K.-S., & Lumley, J. L. (2001). The return to isotropy of homogeneous turbulence. *Journal of Fluid Mechanics*, *436*, 59–84.

Deshpande, R., de Silva, C. M., & Marusic, I. (2023). Evidence that superstructures comprise self-similar coherent motions in high Reynolds number boundary layers. *Journal of Fluid Mechanics*, *969*, A10.

Dougherty, J. (1961). The anisotropy of turbulence at the meteor level. *Journal of Atmospheric and Terrestrial Physics*, *21*(2-3), 210–213.

Durbin, P. (1993). A Reynolds stress model for near-wall turbulence. *Journal of Fluid Mechanics*, *249*, 465–498.

Everard, K., Katul, G., Lawrence, G., Christen, A., & Parlange, M. (2021). Sweeping effects modify Taylor's frozen turbulence hypothesis for scalars in the roughness sublayer. *Geophysical Research Letters*, *48*(22), e2021GL093746.

Freire, L. S., Dias, N. L., & Chamecki, M. (2019). Effects of path averaging in a sonic anemometer on the estimation of turbulence-kinetic-energy dissipation rates. *Boundary-Layer Meteorology*, *173*(1), 99–113.

Garratt, J. (1992). *The atmospheric boundary layer*. Cambridge University Press, Cambridge, Great Britain.

Grachev, A. A., Andreas, E. L., Fairall, C. W., Guest, P. S., & Persson, P. O. G. (2015). Similarity theory based on the Dougherty–Ozmidov length scale. *Quarterly Journal of the Royal Meteorological Society*, *141*(690), 1845–1856.

Guo, H., Golaz, J.-C., Donner, L., Wyman, B., Zhao, M., & Ginoux, P. (2015). CLUBB as a unified cloud parameterization: Opportunities and challenges. *Geophysical Research Letters*, *42*(11), 4540–4547.

Hanjalić, K., & Launder, B. (2021). Reassessment of modeling turbulence via Reynolds averaging: A review of second-moment transport strategy. *Physics of Fluids*, *33*(9), 091302.

Horst, T., & Oncley, S. (2006). Corrections to inertial-range power spectra measured by csat3 and solent sonic anemometers, 1. path-averaging errors. *Boundary-Layer Meteorology*, *119*(2), 375–395.

Hsieh, C.-I., & Katul, G. G. (1997). Dissipation methods, Taylor's hypothesis, and stability correction functions in the atmospheric surface layer. *Journal of Geophysical Research: Atmospheres*, *102*(D14), 16391–16405.

Huang, K. Y., Brunner, C. E., Fu, M. K., Kokmanian, K., Morrison, T. J., Perelet, A. O., ... Hultmark, M. (2021). Investigation of the atmospheric surface layer using a novel high-resolution sensor array. *Experiments in Fluids*, *62*(4), 76.

Huang, K. Y., Fu, M. K., Byers, C. P., Bragg, A. D., & Katul, G. G. (2023). Logarithmic scaling of higher-order temperature moments in the atmospheric surface layer. *International Journal of Heat and Fluid Flow*, *102*, 109162.

Huang, K. Y., & Katul, G. G. (2022). Profiles of high-order moments of longitudinal velocity explained by the random sweeping decorrelation hypothesis. *Physical Review Fluids*, *7*(4), 044603.

Huang, K. Y., Katul, G. G., & Hultmark, M. (2021). Velocity and temperature dissimilarity in the surface layer uncovered by the telegraph approximation. *Boundary-Layer Meteorology*, *180*(3), 385–405.

Hunt, J., & Carlotti, P. (2001). Statistical structure at the wall of the high reynolds number turbulent boundary layer. *Flow, Turbulence and Combustion*, *66*(4), 453–475.

Hutchins, N., Chauhan, K., Marusic, I., Monty, J., & Klewicki, J. (2012). Towards reconciling the large-scale structure of turbulent boundary layers in the atmosphere and laboratory. *Boundary-layer meteorology*, *145*(2), 273–306.

Kader, B., & Yaglom, A. (1990). Mean fields and fluctuation moments in unstably stratified turbulent boundary layers. *Journal of Fluid Mechanics*, *212*, 637–662.

Kader, B., & Yaglom, A. (1991). Spectra and correlation functions of surface layer atmospheric turbulence in unstable thermal stratification. In *Turbulence and coherent structures* (pp. 387–412). Springer.

Kader, B., Yaglom, A., & Zubkovskii, S. (1989). Spatial correlation functions of surface-layer atmospheric turbulence in neutral stratification. *Boundary-Layer Meteorology*, *47*(1), 233–249.

Kaimal, J., & Finnigan, J. J. (1994). *Atmospheric boundary layer flows: Their structure and measurement*. Oxford University Press.

Kaimal, J., Wyngaard, J., & Haugen, D. (1968). Deriving power spectra from a three-component sonic anemometer. *Journal of Applied Meteorology and Climatology*, *7*(5), 827–837.

Kaimal, J., Wyngaard, J., Izumi, Y., & Coté, O. (1972). Spectral characteristics of surface-layer turbulence. *Quarterly Journal of the Royal Meteorological Society*, *98*(417), 563–589.

Katul, G., & Hsieh, C.-I. (1997). Reply to the comment by bink and meesters. *Boundary-Layer Meteorology*, *84*(3), 503–509.

Katul, G., Hsieh, C.-I., & Sigmon, J. (1997). Energy-inertial scale interactions for velocity and temperature in the unstable atmospheric surface layer. *Boundary-Layer Meteorology*, *82*(1), 49–80.

Katul, G., Li, D., Chamecki, M., & Bou-Zeid, E. (2013). Mean scalar concentration profile in a sheared and thermally stratified atmospheric surface layer. *Physical Review E*, *87*.

Katul, G. G., Chu, C. R., Parlange, M. B., Albertson, J. D., & Ortenburger, T. A. (1995). Low-wavenumber spectral characteristics of velocity and temperature in the atmospheric surface layer. *Journal of Geophysical Research: Atmospheres*, *100*(D7), 14243–14255.

Katul, G. G., Porporato, A., Manes, C., & Meneveau, C. (2013). Co-spectrum and mean velocity in turbulent boundary layers. *Physics of Fluids*, *25*(9), 091702.

Katul, G. G., Porporato, A., Shah, S., & Bou-Zeid, E. (2014). Two phenomenological constants explain similarity laws in stably stratified turbulence. *Physical Review E*, *89*(2), 023007.

Kays, W. M. (1994). Turbulent Prandtl number. where are we? *ASME Journal of Heat Transfer*, *116*(2), 284–295.

Large, W. G., McWilliams, J. C., & Doney, S. C. (1994). Oceanic vertical mixing: A review and a model with a nonlocal boundary layer parameterization. *Reviews of Geophysics*, *32*(4), 363–403.

Launder, B., Reece, G., & Rodi, W. (1975). Progress in the development of a Reynolds-stress turbulence closure. *Journal of Fluid Mechanics*, *68*, 537–566.

Li, D. (2019). Turbulent prandtl number in the atmospheric boundary layer-where are we now? *Atmospheric Research*, *216*, 86–105.

Li, D., Salesky, S. T., & Banerjee, T. (2016). Connections between the ozmidov scale and mean velocity profile in stably stratified atmospheric surface layers. *Journal of Fluid Mechanics*, *797*, R3.

Lumley, J. (1965). Interpretation of time spectra measured in high-intensity shear flows. *Physics of Fluids*, *8*(6), 1056–1062.

Lumley, J. (1967). Similarity and the turbulent energy spectrum. *Physics of Fluids*, *10*, 855–858.

Lumley, J. L. (1979). Computational modeling of turbulent flows. *Advances in Applied Mechanics*, *18*, 123–176.

Mellor, G. L., & Yamada, T. (1982). Development of a turbulence closure model for geophysical fluid problems. *Reviews of Geophysics*, *20*(4), 851–875.

Metzger, M. M. (2002). *Scalar dispersion in high reynolds number turbulent boundary layers*. The University of Utah.

Monin, A. S., & Obukhov, A. M. (1954). Basic laws of turbulent mixing in the surface layer of the atmosphere. *Contrib. Geophys. Inst. Acad. Sci. USSR*, *151*(163), e187.

Morrison, T., Calaf, M., Higgins, C. W., Drake, S. A., Perelet, A., & Pardyjak, E. (2021). The impact of surface temperature heterogeneity on near-surface heat transport. *Boundary-Layer Meteorology*, *180*(2), 247–272.

Mortarini, L., Katul, G., Mauricio Cely-Toro, I., Quaresma Dias-Júnior, C., & Mammarella, I. (2025). The role of thermal stratification on the co-spectral properties of momentum transport above an amazonian forest. *Quarterly Journal of the Royal Meteorological Society*, e5024.

Panofsky, H., & Mares, E. (1968). Recent measurements of cospectra for heat-flux and stress. *Quarterly Journal of the Royal Meteorological Society*, *94*(402), 581–585.

Pope, S. (2000). *Turbulent flows*. Cambridge, UK: Cambridge University Press.

Priestley, M. B. (1988). *The spectral analysis of time series.* Oxford University Press.

Stiperski, I., Katul, G. G., & Calaf, M. (2021). Universal return to isotropy of inhomogeneous atmospheric boundary layer turbulence. *Physical Review Letters*, *126*(19), 194501.

Taylor, G. I. (1938). The spectrum of turbulence. *Proceedings of the Royal Society of London. Series A-Mathematical and Physical Sciences*, *164*(919), 476–490.

Tennekes, H., & Lumley, J. (1972). *A first course in turbulence*. Cambridge, MA: MIT Press.

Wilczak, J., & Businger, J. A. (1984). Large-scale eddies in the unstably stratified atmospheric surface layer. part ii: Turbulent pressure fluctuations and the budgets of heat flux, stress and turbulent kinetic energy. *Journal of Atmospheric Sciences*, *41*(24), 3551–3567.

Wyngaard, J., & Clifford, S. (1977). Taylor's hypothesis and high–frequency turbulence spectra. *Journal of Atmospheric Sciences*, *34*(6), 922–929.

Wyngaard, J., & Coté, O. (1972). Cospectral similarity in the atmospheric surface layer. *Quarterly Journal of the Royal Meteorological Society*, *98*(417), 590–603.

Wyngaard, J. C. (2010). *Turbulence in the atmosphere*. Cambridge University Press.

Zeman, O., & Lumley, J. L. (1976). Modeling buoyancy driven mixed layers. *Journal of Atmospheric Sciences*, *33*(10), 1974–1988.

Zilitinkevich, S. (1973). Shear convection. *Boundary-Layer Meteorology*, *3*(4), 416–423.

Zilitinkevich, S., Gryanik, V. M., Lykossov, V., & Mironov, D. (1999). Third-order transport and nonlocal turbulence closures for convective boundary layers. *Journal of the Atmospheric Sciences*, *56*(19), 3463–3477.